Icarus 286 (2017) 314–329

Contents lists available at ScienceDirect

Icarus

journal homepage: www.elsevier.com/locate/icarus

Goldstone radar evidence for short-axis mode non-principal-axis rotation of near-Earth asteroid (214869) 2007 PA8

Marina Brozović[a,*], Lance A.M. Benner[a], Christopher Magri[b], Daniel J. Scheeres[c], Michael W. Busch[d], Jon D. Giorgini[a], Michael C. Nolan[e], Joseph S. Jao[a], Clement G. Lee[a], Lawrence G. Snedeker[f], Marc A. Silva[f], Kenneth J. Lawrence[a], Martin A. Slade[a], Michael D. Hicks[a], Ellen S. Howell[e], Patrick A. Taylor[g], Juan A. Sanchez[h], Vishnu Reddy[h], Melissa Dykhuis[h], Lucille Le Corre[i]

[a] Jet Propulsion Laboratory, California Institute of Technology, Pasadena, CA 91109-8099, USA
[b] University of Maine at Farmington, Preble Hall, Farmington, ME 04938, USA
[c] Aerospace Engineering Sciences, University of Colorado, Boulder, CO 80309-0429, USA
[d] SETI Institute, Mountain View, CA 94043, USA
[e] The University of Arizona, Tucson, AZ 85721, USA
[f] SAITECH, Goldstone Deep Space Communication Complex, Fort Irwin, CA 92310-5097, USA
[g] Arecibo Observatory, Universities Space Research Association, Arecibo, PR 00612, USA
[h] Lunary and Planetary Laboratory, University of Arizona, Tucson, USA
[i] Planetary Science Institute, Tucson, AZ 85719, USA

ARTICLE INFO

Article history:
Received 19 February 2016
Revised 23 September 2016
Accepted 9 October 2016
Available online 14 October 2016

Keywords:
Asteroids
Rotation
Radar observations

ABSTRACT

We report radar and optical photometric observations of near-Earth asteroid (214869) 2007 PA8 obtained during October 2–November 13, 2012. We observed 2007 PA8 on sixteen days with Goldstone (8560 MHz, 3.5 cm) and on five days with the 0.6 m telescope at Table Mountain Observatory. Closest approach was on November 5 at a distance of 0.043 au. Images obtained with Goldstone's new chirp system achieved range resolutions as fine as 3.75 m, placing thousands of pixels on the asteroid's surface, and revealing that 2007 PA8 is an elongated, asymmetric object. Surface features include angularities, facets, and a concavity approximately 400 m in diameter. We used the *Shape* software to estimate the asteroid's 3D shape and spin state. 2007 PA8 has a broad, rounded end and a tapered, angular end with sharp-crested ridges. The asteroid's effective diameter is 1.35 ± 0.07 km, which in combination with the absolute magnitude of 16.30 ± 0.52 gives an optical albedo of $p_V = 0.29 \pm 0.14$. The shape modeling of the radar data revealed that 2007 PA8 is a non-principal axis (NPA) rotator in the short-axis mode with an average period of precession by the long axis around the angular momentum vector of 4.26 ± 0.02 days and an oscillatory period around the long axis of 20.55 ± 3.75 days. The amplitude of rolling around the long axis is $42 \pm 7°$. The angular momentum vector points toward ecliptic longitude and latitude of $273.6 \pm 10°$, $+16.9 \pm 5°$. 2007 PA8 is only the second confirmed short-axis mode NPA rotator known in the near-Earth asteroid population after (99942) Apophis (Pravec et al., 2014). 2007 PA8 has a geopotential high at the equator, where the equator is defined as the plane that contains the long and intermediate axis. This geopotential extreme could be interpreted as a large, hidden surface depression, or as evidence that 2007 PA8 is a multi-component body.

© 2016 Elsevier Inc. All rights reserved.

1. Introduction

Near-Earth asteroid (214869) 2007 PA8 was discovered by MIT's Lincoln Laboratory LINEAR survey on August 9, 2007 and is classified as a "Potentially Hazardous Asteroid" by the Minor Planet Center. 2007 PA8 has an unusual orbit (semi major axis = 2.823 au, eccentricity = 0.662, inclination = 1.98°, perihelion distance = 0.955 au, aphelion distance = 4.692 au) that resembles those of Jupiter-family comets. 2007 PA8 has a Tisserand parameter of T = 2.947, which is below the threshold of T = 3.0 that is often thought to separate asteroidal (T > 3.0) from cometary (T < 3.0) orbits. For the time period between 1900 and 2100, JPL's Horizons on-line solar system data and ephemeris computation service (http://ssd.jpl.nasa.gov/horizons.cgi, Giorgini et al., 1996) lists

* Corresponding author. Fax: 818 393 7116.
E-mail address: marina.brozovic@jpl.nasa.gov (M. Brozović).

http://dx.doi.org/10.1016/j.icarus.2016.10.016
0019-1035/© 2016 Elsevier Inc. All rights reserved.

Table 1
Lightcurve observations from Table Mountain Observatory in October of 2012.

Date	Time range START	(UTC) STOP	RA (°)	Dec (°)	Apmag (mag)	Distance (au)	SOT (°)	TOM (°)	Illu. (°)	Filters
Oct 2	04:57	07:33	13.9	−2.1	14.3	0.241	172.1	23.3	95.6	R
Oct 17	06:06	10:20	20.5	−7.3	13.1	0.132	163.2	143.4	4.8	BVRI
Oct 28	05:47	09:37	38.7	−17.3	11.9	0.068	148.9	35.4	97.8	BVRI
Oct 30	06:50	09:56	46.2	−20.4	11.8	0.059	143.9	37.5	99.8	R
Oct 31	06:58	09:48	51.1	−22.2	11.7	0.055	140.6	41.0	98.0	R

The times show the start and stop times for each lightcurve. RA and Dec are J2000.0 astrometric right ascension and declination of 2007 PA8 center in mid-epoch of observations. We also list the asteroid's approximate apparent visual magnitude (Apmag) from the standard IAU H-G magnitude relationship, distance from Earth in au, Sun-Observer-Target (SOT) angle, Target-Observer-Moon (TOM) angle, and percentage of the Moon's illumination (Illu.). The last column shows the filters used on each day. We used lightcurves from R-band photometry (effective wavelength 0.63 μm) in our analysis.

six < 0.1 au approaches of 2007 PA8 to Earth and four to Mars. In addition, there are also eight 1.5–2.0 au approaches to Jupiter. 2007 PA8 is one of several dozen near-Earth asteroids (NEAs) with comet-like orbits that have been detected with radar.

Nedelcu et al. (2014) obtained near infrared (NIR) spectra (0.8–2.5 μm) of 2007 PA8 with NASA's Infrared Telescope Facility (IRTF). By comparison with meteorite spectra they found that the best fit for the spectrum of 2007 PA8 corresponded to an H5 ordinary chondrite. Fornasier et al. (2015) acquired visible and NIR spectra (0.38–2.4 μm) using the Telescopio Nazionale Galileo (TNG). From the mineralogical analysis they concluded that 2007 PA8 has a composition consistent with L chondrites, and identified the Gefion family as the most likely source region. Sanchez et al. (2015) obtained NIR spectra (~0.7–2.55 μm) with the IRTF and their analysis has shown that 2007 PA8's composition is consistent with olivine ($Fa_{18}(Fo_{82})$) and pyroxene (Fs_{16}), with an olivine abundance of 47%. These values are consistent with an H ordinary chondrite classification. Moreover, Sanchez et al. (2015) found a possible affinity with either H4 or H5 chondrites, suggesting that 2007 PA8 could have originated in the interior of a larger body that experienced some degree of thermal metamorphism.

On November 5, 2012, 2007 PA8 approached the Earth within 0.0433 au (16.8 lunar distances), the closest encounter by this asteroid for at least one hundred years. We organized an extensive observing campaign at radar and optical wavelengths during October and November to characterize it. Although nothing was known about the object's physical properties prior to the flyby, the absolute magnitude $H_v = 16.4$ (Minor Planet Center database, http://www.minorplanetcenter.net/iau/MPCORB/MPCORB.DAT) suggested a diameter within a factor of two of 1.8 km. Here we describe shape and spin state estimation from inversion of the radar data. We find that 2007 PA8 is in an excited, short axis mode (SAM) spin state, similar to that of (99942) Apophis (Pravec et al., 2014), the only other SAM rotator currently known in the near-Earth asteroid population.

2. Observations and data reduction

2.1. Photometric observations

We observed 2007 PA8 with the 0.6 m telescope at Table Mountain Observatory on 5 days between October 2 and 31. The observing conditions were not ideal, given that the object was between 23 and 41° from a nearly full Moon on four of the nights. The optical observations are summarized in Table 1. The photometric data were reduced with IRAF and custom built software (Hicks et al., 2014).

The lightcurves showed small magnitude variations over several hours of photometric observations and hinted at slow rotation. The longest lightcurve was obtained on October 17. It covers 4.23 h during which the brightness changed by ~0.3 mag. A Fourier analysis that yielded a rotational period of 95.1 ± 3.4 h was reported in Hicks et al. (2012a). The large uncertainty is due to the sparse data set.

2.2. Radar observations

We observed 2007 PA8 at Goldstone (8560 MHz, 3.5 cm) on 16 days between October 16 and November 13, 2012 (Table 2) as the asteroid traversed ~120° across the sky. The asteroid was too far south for observations at Arecibo during this apparition. The SNRs on October 16 were much stronger than expected and enabled coarse resolution imaging. The closest approach occurred on November 5 at 0.043 au with signal-to-noise ratios (SNRs) of several thousand per day that were suitable for the highest resolution imaging possible at Goldstone. The observations concluded on November 13, when 2007 PA8 was outbound at 0.065 au.

We used three observational setups: Doppler-only, binary phase coded (BPC) waveforms for ranging and intermediate resolution imaging, and linear frequency modulation (LFM) or chirp waveforms for high resolution imaging. During Doppler-only observations, we transmit a circularly polarized electromagnetic wave of constant amplitude and frequency. The wave reflects off the surface and the target's rotation spreads the signal in Doppler frequency. The Doppler broadening of the echo is a function of the asteroid's rotation period, diameter, and spin axis orientation with respect to the radar-line-of sight (Ostro, 1993):

$$B = \frac{4\pi D}{\lambda P}\cos(\delta) \quad (1)$$

where B is the echo bandwidth, P is the rotation period, D is the object's diameter, λ is the radar wavelength, and δ is the subradar latitude.

The reflected wave returns in the same sense of circular polarization (SC) as the outgoing beam and in the opposite sense (OC). Echoes from a surface that is smooth at decimeter scales will return almost entirely in the OC channel. SC echoes can result from multiple scattering from rough surfaces, single scattering from surfaces with radii of curvature comparable to the radar wavelength, and from coherent backscattering. The ratio of the two echoes, SC/OC, is a proxy for the target's near-surface complexity or roughness.

Binary phase coded and chirp waveforms are used for ranging and delay-Doppler imaging. With BPC observations, we continuously transmit a circularly polarized electromagnetic wave as in Doppler-only observations, but the transmitted signal is phase-modulated via a repeating pseudo-random binary code. We use BPC observations in order to achieve resolutions up to 18.75 m. The chirping setup utilizes linear frequency modulation (Slade at al., 2011; Quirk and Srinivasan, 2013) as an alternative way to modulate the carrier wave. This method allows us to utilize the full 40 MHz bandwidth of Goldstone's klystron amplifiers. Chirping at 40 MHz gives a range resolution of 3.75 m.

We used data reduction techniques that were nearly identical to those described in Magri et al. (2007). During the observations,

Table 2
Masterlog of Goldstone radar observations in October and November of 2012.

Date	Time range (UTC)	Setup	Resolution		Code	Runs	RA	Dec	Distance	Sol
	START STOP		(μs)	(Hz)			(°)	(°)	(au)	
Oct 16	06:37:10–07:02:54	Doppler-only	–	0.100	–	6	20	−7	0.139	69
	07:15:26–07:31:44	BPC	10	6.152	127	4				69
	07:40:35–07:52:09	BPC	11	5.592	127	3				69
	08:10:17–09:37:01	BPC	1	0.120	255	19				71
Oct 17	06:43:14–07:12:06	Doppler-only	–	0.100	–	7	21	−7	0.133	73
	07:23:54–08:28:21	BPC	1	0.060	127	15				73
Oct 18	05:44:13–06:16:40	Doppler-only	–	0.100	–	5	21	−8	0.126	75
	06:26:50–09:19:36	BPC	1	0.060	127	41				75
Oct 19	06:11:04–06:29:17	Doppler-only	–	0.050	–	5	22	−8	0.120	77
	06:42:28–09:11:07	BPC	0.5	0.060	127	37				77
Oct 28	06:20:10–06:28:17	Doppler-only	–	0.050	–	4	39	−17	0.068	79
	06:46:45–06:59:27	BPC	1	0.479	255	6				79
	07:10:13–07:32:20	BPC	0.25	0.032	127	10				81
	07:39:34–11:10:43	BPC	0.125	0.016	255	91				81
Oct 29	05:06:08–05:15:51	Doppler-only	–	0.050	–	5	42	−19	0.064	81
	05:23:33–08:00:39	BPC	0.125	0.018	255	73				81
Oct 30	08:16:02–08:24:58	Doppler-only	–	0.050	–	5	47	−21	0.058	83
	08:29:59–11:14:56	BPC	0.125	0.020	255	83				83
Oct 31	05:51:05–05:59:31	Doppler-only	–	0.050	–	5	51	−22	0.055	85
	06:08:21–07:35:11	BPC	0.125	0.021	255	46				85
Nov 02	07:00:56–07:08:15	Doppler-only	–	0.050	–	5	64	−26	0.048	87
	07:16:58–07:49:27	BPC	0.125	0.024	255	20				87
	08:37:32–09:49:11	Chirp	0.05	0.025	1000	44				87
Nov 03	08:11:18–08:18:16	Doppler-only	–	0.050	–	5	72	−28	0.046	89
	08:26:36–11:10:36	Chirp	0.05	0.025	1000	106				89
Nov 05	09:15:00–09:45:00	Doppler-only speckle with Pie Town and Los Alamos								
	11:10:48–11:49:36	Chirp	0.025	0.028	2000	20	90	−30	0.043	91
	11:56:48–12:35:36	Chirp	0.05	0.028	1000	20				91
Nov 06	10:15:00–10:45:00	Doppler-only speckle with Pie Town and Los Alamos								
	11:05:07–11:39:39	Chirp	0.025	0.028	2000	24	100	−30	0.043	91
Nov 08	10:30:00–11:00:00	Doppler-only speckle with Pie Town, Los Alamos, and VLA								
	11:09:04–13:19:32	Chirp	0.05	0.025	1000	82	118	−28	0.047	93
Nov 11	10:56:03–11:04:39	Doppler-only	–	0.050	–	5	137	−23	0.056	95
	11:13:13–14:05:06	BPC	0.125	0.020	255	90				95
Nov 12	11:01:05–11:10:18	Doppler-only	–	0.050	–	5	142	−21	0.060	95
	11:22:27–12:44:01	BPC	0.125	0.019	255	40				95
Nov 13	11:06:10–11:59:29	BPC	0.125	0.018	255	25	145	−20	0.065	97

Observations were conducted monostatically at X-band (8560 MHz, 3.5 cm) with an average transmitter power of 450 kW. The echoes were received in SC and OC polarizations. The times show the start and end of the reception of echoes for each setup on each day. The data resolution is given in time delay or baud (μs) and Doppler frequency (Hz). "Code" refers to the length of the repeating binary phase code or the pulse length for chirped imaging. The "ranging" data represent coarse imaging data that were used for the first-order orbital improvements. Right ascension, declination, and distance (in au) are given at the beginning of each observation session. We also list the number of transmit-receive cycles (runs) and the orbital solution (Sol) used to compute delay-Doppler ephemeris predictions.

each run consists of a radio signal transmitted for the duration of the round-trip-time (RTT) between the observer and the target, followed by reception of the echo for the same duration less the time required to switch from transmit to receive. The data collected during one run are processed with Fast Fourier Transforms (FFTs) of a certain length that defines the Doppler resolution. If we use the entire receive duration of a run to resolve the data, then we have a single measurement, or "look" per run. If we use an FFT length that is shorter, giving coarser Doppler resolution, then we can obtain more statistically independent measurements (N_{looks}) per run. The data from different runs are combined into incoherent sums in order to reduce the fractional noise fluctuation by $\sqrt{\sum_{runs} N_{looks}}$.

Fig. 1 shows echo power spectra obtained on each day. Spectra obtained on October 16, 18, and 31 have an asymmetric appearance, the data from October 17 and November 12 show a central dip, and the OC spectrum on October 29 shows a large spike, possibly from a specular glint. The bandwidth changed significantly from day to day, either due to the asteroid's elongation, a change in subradar latitude, or both. We estimated bandwidths visually by measuring the width of the OC spectra where the signal was at least three standard deviations above the noise level. The maximum and minimum bandwidths were 1.5 Hz on October 16 and 0.9 Hz on November 3.

We also conducted radar speckle tracking (Busch et al., 2010) observations on November 5, 6, and 8 in an attempt to constrain the spin state. The speckle experiment used Goldstone to transmit and Pie Town, Los Alamos, and elements of the Very Large Array (VLA) as the receiving stations. As the asteroid spins, its radar speckle pattern passes over one receiving antenna and then the other, producing a time lag. We obtained usable time lag measurements on November 5 and 6 (Fig. 2). The time lags between Los Alamos and Pie Town were -1.1 ± 0.3 s at 2012 Nov. 5 09:30 UTC and -1.4 ± 0.5 s at 2012 Nov. 6 10:30 UTC. The time lags are consistent with either retrograde rotation or with a range of pole directions with high-obliquities, but they do not provide enough information for more stringent constraints on the spin state.

The delay-Doppler images resolve the echo in range and provide lower bounds on the object's size. The first delay-Doppler image from October 16 was obtained by integrating 1 μs (150 m resolution) data for almost 1.5 h. The echo is asymmetric and has a visible extent of ~600 m. Asymmetry was also evident in the echo power spectrum from the same day (Fig. 1). Images obtained on

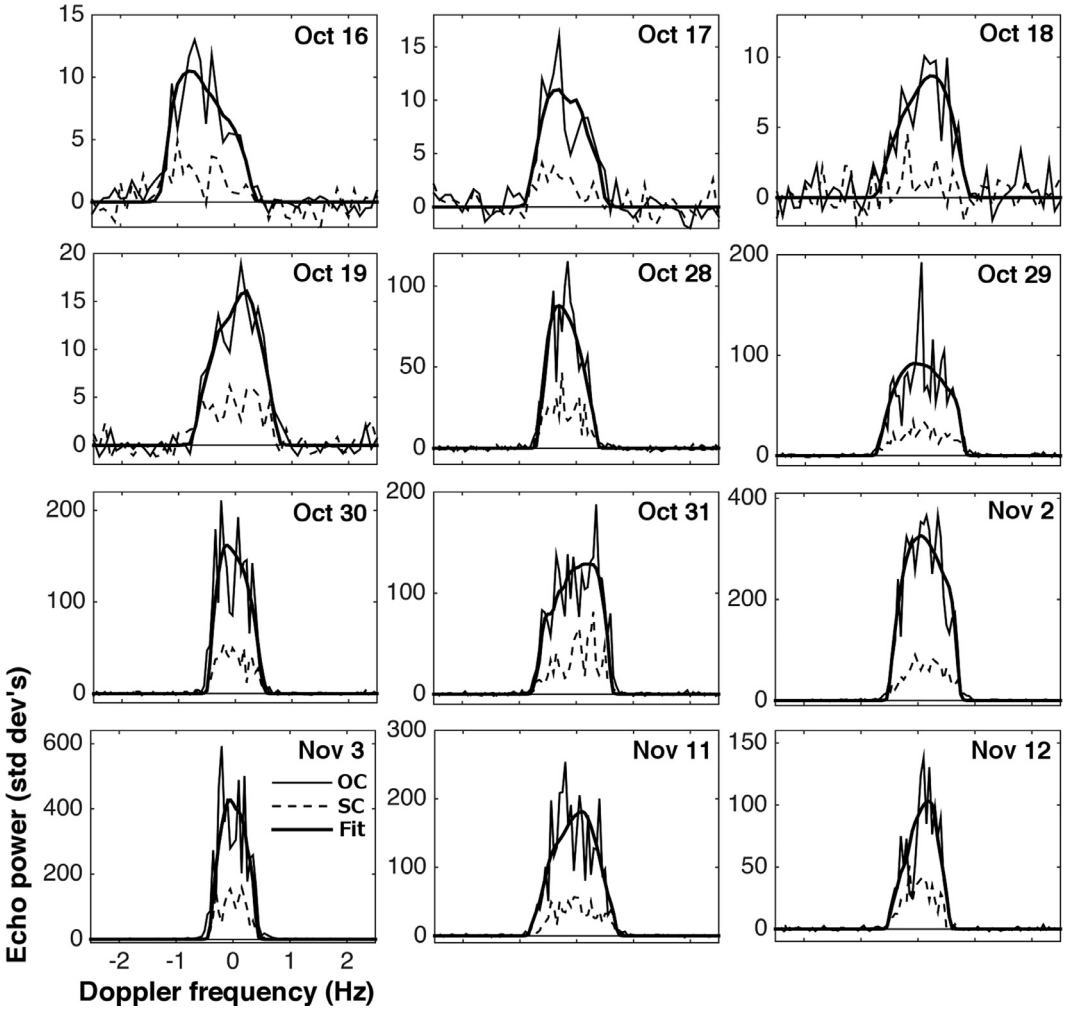

Fig. 1. OC (thin solid line) and SC (dashed line) echo power spectra. Each spectrum is a daily sum with start-stop times listed in Table 2, except for October 18, when the sum spans the interval between 05:44:13 and 05:54:45 UTC. The observations from October 16 to 19 have a Doppler resolution of 0.1 Hz and others have a resolution of 0.05 Hz. In chronological order, the number of looks in each spectrum are 78, 84, 36, 55, 12, 10, 10, 10, 10, 10, 10, 10, respectively. The thick solid line represents the shape model fits to the OC spectra discussed in Section 3.5.

October 17, 18, and 19 provided clear evidence that 2007 PA8 is a moderately elongated object with a rotation period slow enough that a 1.5 h integration did not produce excessive rotational smearing. By late October, 2007 PA8 was significantly closer and the SNRs were much stronger. Imaging during the rest of the campaign used range resolutions between 18.75 m and 3.75 m.

Fig. 3A and B show high-resolution delay-Doppler images and Table 3 lists their visible extents and bandwidths. The bandwidth of 2007 PA8 is consistently narrow, so the imaging data were processed with the finest Doppler resolution available, which is determined by the inverse of the round-trip-time less the time needed to switch from transmit to receive ($\sim$ 3 s at Goldstone). Delay-Doppler images from October 28 to 31 (Fig. 3A) show different orientations on each day and the bandwidths alternate between narrow and wide over these four days. The October 28 image has a flat leading edge. In contrast, the October 30 and 31 echoes are angular.

The radar images reveal evidence for at least three relatively large radar-dark features that could be concavities. Feature C1 has a visible extent of at least 200 m in images on October 28 and 31. Feature C2 has a visible extent of at least 300 m in images on October 28 and 29. Feature C3 has a visible extent of at least 600 m in images on October 30 and 31. All radar-dark features are outlined by bright pixels, suggesting that the surrounding surface is elevated and/or includes surfaces oriented closer to normal to the line of sight, thus making them more reflective. The radar-dark areas could also be interpreted as areas that are less reflective due to lower density, but concavities seem more likely given that they have been observed on the surfaces of (433) Eros and (4179) Toutatis in spacecraft images (Veverka et al., 2000; Huang et al., 2013). Features C2 and C3 rotate $\sim$90° between consecutive days and suggest a rotation period of $\sim$4 days, which is consistent with the period estimated from photometry. The orientation of the asteroid seen on November 2 closely resembles the asteroid's appearance on October 29, including feature C2 in a similar position in the image.

Starting on November 3, features become more difficult to identify between the early and later dates. For example, images obtained on October 30 and November 3 appear to show the asteroid in a similar orientation, and although the echo outline has a similar elongated and angular appearance, formerly prominent feature C3 is no longer visible on November 3 (Fig. 3A). Similarly, the asteroid's orientation on November 5 (Fig. 3B) does not correspond to the appearance in any of the previous delay-Doppler images and it is not clear if the $\sim$400 m diameter, circular radar-dark feature in Fig. 3B is feature C2 or something else. Fig. 3B also shows three additional radar-dark features that are labeled C4, C5, and C6. These features could be small concavities viewed close to edge-on. Delay-Doppler radar images are non-intuitive and can be difficult to interpret without a 3D shape model of the object. We will show later

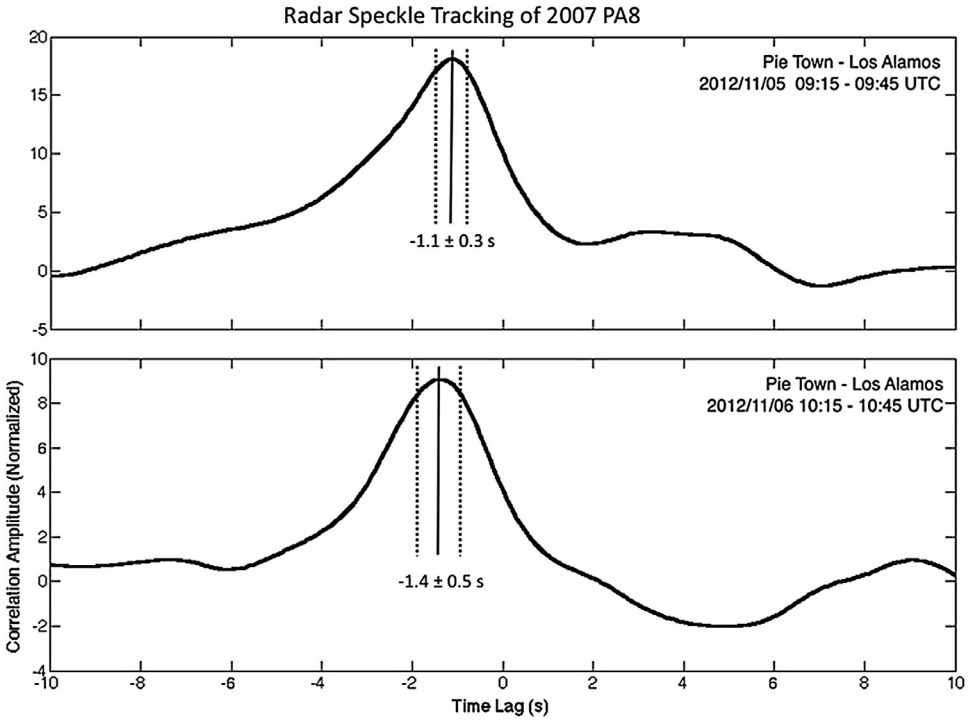

Fig. 2. Radar speckle tracking observations on November 5 and 6, using the Pie Town and Los Alamos stations of the Very Long Baseline Array. The plots show the normalized correlation amplitude of the radar echo power received by Pie Town with that received by Los Alamos for a range of time lags during each speckle tracking session. The peaks indicate the true time lag of the speckle pattern. Negative time lags mean that a given part of the speckle pattern arrived at Pie Town first.

in shape modeling that the radar-dark features do correspond to concavities.

We searched the highest resolution and strongest SNR images for persistent radar-bright spots that could suggest boulders but did not find compelling evidence for any. Our search included animating sequences of images from the longest tracks to search for small bright features that moved in a regular pattern as the asteroid rotates. This approach has led to discovery of boulder candidates on other near-Earth asteroids such as Toutatis and (341843) 2008 EV5 (Benner et al., 2015). With 2007 PA8, little rotation is evident within radar images from a given day (e.g. Supplementary Fig. 1), and this approach did not reveal any candidate boulders.

3. Shape modeling

We used the *Shape* software (Hudson 1994; Magri et al., 2007) which utilizes a constrained, weighted least-squares minimization procedure to search for the best set of model parameters to describe a target object's shape, size, spin state, and radar and optical scattering properties. *Shape's* algorithm steps though the parameter space by sequentially adjusting individual parameters to decrease χ^2. In delay-Doppler space, the size, pole direction, and spin rate are correlated, and can be difficult to untangle unless an extensive data set is available. Even if good rotational coverage and a variety of observing geometries are available, user involvement in the parameter optimization is essential to prevent non-physical fits.

The shape modeling data set consists of 12 echo power spectra and 45 delay-Doppler images, covering 16 days from October 16 to November 13 (see Supplementary Table 1). Each spectrum or image has an integration time between 10 min and 1.4 h. We incoherently summed as many runs as possible in order to maximize the SNRs, while also keeping rotational smear to a minimum. For time-delay resolutions between 0.125 μs and 1.0 μs, we summed data so that rotational smear was $\leq 10°$ ($\sim$ 2.7 h), but for fine delay resolutions of 0.05 μs and 0.025 μs, we summed data spanning $\leq 5°$ of rotation ($\sim$ 1.3 h).

The lightcurves were added to the shape modeling dataset only after we have already achieved a good fit to the radar data. This was done because the *Shape* software handles lightcurves in a computationally costly manner and because all lightcurves except on October 2 overlapped the much stronger radar data. This approach has been used successfully with several other NEAs previously (Hudson et al., 1997; Hudson and Ostro 1998; Bush et al. 2006; Magri et al., 2007).

3.1. Constraining the size and spin state

The visible extents in Table 3 provided a first order size constraint for 2007 PA8. Using the maximum and minimum visible extents, we started with a 2.30 km × 1.05 km × 1.05 km ellipsoid. However, given the irregular shapes of the radar echoes, and likely off-the-equator viewing geometries, we allowed the dimensions to vary during the fit. The initial search for a spin state assumed principal axis rotation. The pole direction was assigned fixed values in increments of 15° in ecliptic longitude, λ, and latitude, β. The sidereal rotation rate was assigned fixed values from 80 to 100°/day, corresponding to periods between 3.6 days and 4.5 days, in steps of 5°/day. A spin rate of 85°/day (period $\sim$ 102 h) produced the best fits.

The candidate poles clustered within either 10° of the south ecliptic pole (retrograde pole) or around ecliptic longitude and latitude $\lambda = 270°$, $\beta = +15°$ (high-obliquity pole). The speckle tracking results (Supplementary Fig. 2) start to exclude the pole around $\beta = -90°$ for periods > 100 h, but in these initial stages of shape modeling, we decided to proceed with both pole regions.

We proceeded with a more sophisticated search using a shape described by 10th order spherical harmonics (Magri et al., 2007). The spin rate was allowed to vary. Representative harmonic fits

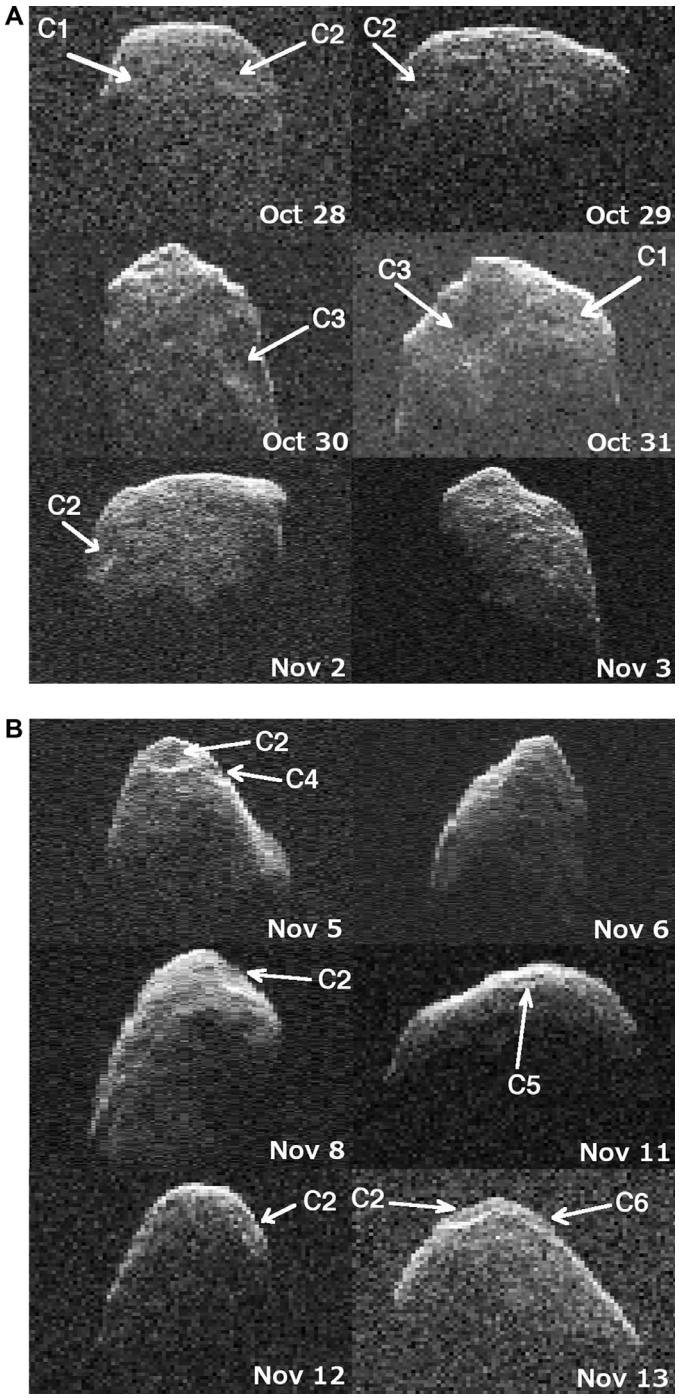

Fig. 3. High-resolution delay-Doppler images. Time delay (distance) increases from top to bottom and Doppler frequency increases from left to right. The vertical dimension of each image is 1.5 km and the horizontal dimension is 1.9 Hz. The images are normalized so that the noise has zero mean and unit standard deviation. The white arrows and letters mark features discussed in the text. **A.** Images from October 28 to November 3. **B.** Images from November 5 to 13. The range resolutions are 18.75 m on Oct. 28–31 and Nov. 11–13; 7.5 m on Nov. 2, 3, and 8; and 3.75 m on Nov. 5 and 6 (Table 2).

are shown in Supplementary Fig. 3 and their physical properties are listed in Supplementary Table 2. Overall, the high-obliquity pole model had lower reduced χ^2 than the retrograde pole model ($\chi^2 = 1.145$ vs. 1.185 is a statistically significant result given a number of degrees of freedom in the fit), supporting the conclusion from the speckle tracking. However, even the best harmonic model fits show persistent mismatches with the data.

Table 3
Doppler bandwidths and visible range extents.

Date	Bandwidth (Hz)	Δf (Hz)	Visible extent (m)	Δd (m)
Oct 16	1.556 ± 0.120	0.120	600 ± 150	150
Oct 17	1.082 ± 0.060	0.060	600 ± 150	150
Oct 18	1.382 ± 0.060	0.060	600 ± 150	150
Oct 19	1.262 ± 0.060	0.060	525 ± 150	75
Oct 28	1.095 ± 0.048	0.016	806 ± 94	19
Oct 29	1.460 ± 0.036	0.018	694 ± 56	19
Oct 30	1.002 ± 0.039	0.020	1031 ± 56	19
Oct 31	1.322 ± 0.042	0.021	938 ± 38	19
Nov 2	1.175 ± 0.050	0.025	728 ± 38	7.5
Nov 3	0.875 ± 0.050	0.025	765 ± 60	7.5
Nov 5	1.083 ± 0.083	0.028	848 ± 38	3.75
Nov 6	0.889 ± 0.083	0.028	994 ± 38	3.75
Nov 8	0.950 ± 0.075	0.025	1148 ± 60	7.5
Nov 11	1.500 ± 0.040	0.020	619 ± 56	19
Nov 12	1.010 ± 0.056	0.019	844 ± 75	19
Nov 13	1.461 ± 0.035	0.018	806 ± 75	19

Doppler bandwidths and visible extents of the echoes estimated from radar images. Δf is the Doppler resolution and Δd is the range resolution. The dimensions were estimated by counting pixels that were either contiguous or nearly contiguous with the rest of the echo and that were at least three standard deviations above the noise level. The uncertainties come from a subjective consideration of whether a pixel is a part of the echo or not.

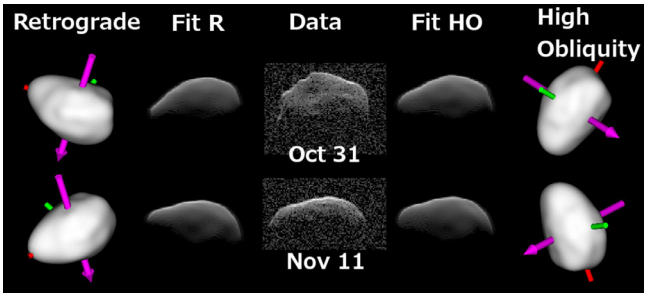

Fig. 4. Fits to the data of October 31 and November 11, generated from two different shape models. Both models are tenth-order spherical harmonic expansions and assume rotation about the short principal axis with a rotation period of ~102 h. The collages show, from left to right: plane-of-sky renderings of the model with a retrograde pole, fits, delay-Doppler radar data, fits for the model with a high obliquity pole, and the high obliquity modeled plane-of-sky renderings. In the data and fits, time delay increases from top to bottom, and Doppler frequency increases from left to right. The plane of sky view is contained in a 2.3 × 2.3 km square with 201 × 201 pixels. The magenta arrow shows the orientation of the spin vector, and red and green shafts denote the positive ends of the long and the intermediate axes. (For interpretation of the references to colour in this figure legend, the reader is referred to the web version of this article.)

The PA spin state solutions put the asteroid in very similar orientations on October 31 and November 11 with a subradar latitude change of less than 10°. However, the radar echoes are dramatically different on these two days (Fig. 4). The delay-Doppler images from October 31 show a very angular leading edge of the echo, but the leading edge looks very smooth and only slightly curved on November 11. This strongly suggests that there is rotation about the long axis and that 2007 PA8 is a non-principal axis (NPA) rotator.

3.2. 2007 PA8 and NPA rotation

In this section, we investigate if the radar data are better described by assuming NPA rotation. We first describe the mathematical formalism of the excited spin states after which we discuss implications and fits to the data.

Non-principal axis rotation is described by three Euler angles (ϕ, θ, ψ) that orient the body in an inertial reference frame at some epoch t_0, by the spin vector **W**, and by the ratios of long, intermediate, and short-axis moments of inertia (I_l/I_s, I_i/I_s). Here

we adopt the Euler angle definition from Samarasinha and A'Hearn (1991) and Samarasinha and Mueller (2015), which is different from the convention used by Hudson and Ostro (1995) to describe the rotation of asteroid (4179) Toutatis. In the Samarasinha and A'Hearn notation, θ is the angle between the angular momentum vector and the long axis, ψ is the rolling angle about the long axis, and ϕ is the phase angle of long axis rotation about the angular momentum vector.

The ratio between the square of the angular momentum M and the total rotational kinetic energy E determines if the object is in an excited rotational state around the long axis (long axis mode or LAM) or short axis (short axis mode or SAM). The LAM rotation state occurs when $I_l/I_s \leq M^2/(2EI_s) \leq I_i/I_s$ and the SAM rotation occurs when $I_i/I_s < M^2/(2EI_s) \leq 1$. When viewed in an inertial frame, an object in a LAM spin state rotates about the long axis with period P_ψ, the long axis rotates about the angular momentum vector at a variable rate with an average period P_ϕ, and the long axis nods (nutates) with period $P_\theta = P_\psi/2$. For comparison, an object in a SAM spin state oscillates (rolls) about the long axis with period P_ψ, the long axis rotates about the angular momentum vector at a variable rate with an average period P_ϕ, and the long axis nods with period $P_\theta = P_\psi$. Hence, the main difference between LAM and SAM NPA rotation is that in SAM the object does not completely rotate about the long axis.

Shape's least squares algorithm optimizes χ^2 one parameter at a time, which makes it susceptible to local minima in the parameter space. Hence, user input is vital for constraining the eight-dimensional spin state that defines NPA rotation. Hudson and Ostro (1995) started their spin state search for Toutatis by orienting the Euler angles "by hand" for each delay-Doppler image, with no consideration of the underlying dynamics. They calculated the moments of inertia from the shape of the object that was approximated by two spheres in contact. Finally, they fit the initial epoch spin rates (W_{l0},W_{i0},W_{s0}) by matching the results of integration of Euler's equations (e.g., Landau and Lifshitz, 1976) to the measured set of angles. This method provided adequate initial conditions for the more sophisticated shape and spin optimization by using *Shape*.

We placed preliminary constraints on the rotation based on the axis lengths from the harmonic models estimated under the assumption of PA rotation. If we assume LAM NPA rotation, then the periods P_ψ and P_ϕ are related by (Samarasinha and A'Hearn, 1991):

$$\frac{P\psi}{P\phi} \geq \left[\sqrt{\frac{\left(L_l^2+L_i^2\right)\left(L_l^2+L_s^2\right)}{\left(L_l^2-L_i^2\right)\left(L_l^2-L_s^2\right)}}-1\right] \tag{2}$$

For SAM, P_ψ and P_ϕ are related by:

$$\frac{P\psi}{P\phi} \geq \left[\sqrt{\frac{\left(L_l^2+L_s^2\right)\left(L_i^2+L_s^2\right)}{\left(L_l^2-L_s^2\right)\left(L_i^2-L_s^2\right)}}\right] \tag{3}$$

The maximum nodding amplitude for SAM is:

$$(A_\theta)_{max} = sin^{-1}\left[\sqrt{\frac{L_i^4-L_s^4}{L_l^4-L_s^4}}\right] \tag{4}$$

Here, L_l, L_i, and L_s are axes of the dynamically equivalent, equal volume ellipsoid (DEEVE) with the same volume and moment-of-inertia ratios as the shape model. We use the dynamical axes obtained from the PA prograde and retrograde models, 1.73 km × 1.18 km × 1.17 km and 1.78 km × 1.24 km × 1.10 km (Supplementary Table 2) and Eq. 2) to conclude that the period of rotation around the long axis (P_ψ) is at least 1.5 times longer than the period of the precession around the angular momentum vector ($P_{\phi)}$. Assuming that P_ϕ is approximately equal to the PA period of 4 days, this places a lower limit on P_ψ for the LAM NPA rotation of ~6 days.

From Eq. (3), the period of oscillatory roll along the long axis ($P_{\psi)}$ is at least 4.3 times longer than the average rotation period about the angular momentum vector ($P_{\phi)}$. P_ϕ is ~4 days which places a lower limit on P_ψ for the SAM NPA rotation of ~17 days. Furthermore, Eq. (4) suggests that the nodding amplitude A_θ is $< 20°$. In the following two subsections, we investigate if the radar data fit better to the SAM or LAM spin state.

3.2.1. SAM NPA spin state fits

A SAM state is characterized by the rolling amplitude A_ψ. A formal definition of A_ψ is:

$$A_\psi = sin^{-1}\left[\sqrt{\frac{I_i\left(I_s-\frac{M^2}{2E}\right)}{\frac{M^2}{2E}\left(I_s-I_i\right)}}\right] \tag{5}$$

As $M^2/(2E) \rightarrow I_s$, $A_\psi \rightarrow 0°$, and a SAM NPA state becomes indistinguishable from pure PA rotation about the short axis. Appropriately, we also find that the rolling period $P_\psi \rightarrow \infty$ in this limit. Samarasinha and A'Hearn (1991) noted that "SAMs with very large rolling amplitudes (~90°) have very high values of P_ψ/P_ϕ (say> 20) and therefore the amount of roll during a rotation cannot be large". SAMs that are close to $M^2/(2E) \rightarrow I_i$ are considered to be in a "quasi pure rotational state" and should be very rare, since such a state is dynamically unstable.

We started the search for A_ψ by manually adjusting the model's orientation at each observation epoch to improve the fits to the data, then asking what the required adjustments tell us about A_ψ. Visual inspection indicated that the asteroid must rotate at least 40° about the long axis in order to dramatically change the appearance of the leading edge between October 31 and November 11. This implied that the lower limit for A_ψ is ~ 20°. The upper limit for A_ψ had to be less than 90° because in that case $P_\psi \gg P_\phi$ and it would have been difficult to detect the amount of rotation that we observe between October 31 and November 11. Thus, our nominal constraint for A_ψ is that it should lie in the range 20–50°. This is consistent with Samarasinha and A'Hearn's statement: "Therefore, for most practical purposes, a SAM is clearly distinct from a pure rotation about the short axis (for the relevant dynamical axial length ratios) only when the rolling amplitude is moderately large (say ~< 45°)."

Following this initial, intuitive inspection of the candidate SAM state, we proceeded with a more statistical approach. We generated 500 variants of the eight-dimensional (ϕ, θ, ψ, W_{l0}, W_{i0}, W_{s0}, I_l/I_s, and I_i/I_s) SAM spin state. We searched for combinations of spin state parameters that result in SAM spin states with P_ϕ between 90 and 110 h and P_ψ between 400 and 600 h. We also selected for an angular momentum direction between 200 and 300° in λ and −40 to +40° in β, an area of sky that encompasses the high-obliquity PA pole (λ = 270°, β = +15°) discussed in Section 3.1.

Supplementary Fig. 4 shows the phase space distribution for all 500 spin states that were found to satisfy the initial selection criteria. The bounds were kept relatively wide in case we missed something in our preliminary search conclusions. We used the ellipsoid model with principal axes of 1.8 × 1.3 × 1.1 km based on the high-obliquity PA shape model from Supplementary Table 2 for all the spin states. The fits were sorted according to the χ^2 value and the 20 best SAM candidate spin states are listed in Supplementary Table 3. The best solution has a statistically better χ^2 than the runner-up (1.268 vs 1.337) and fits that are visually superior.

The spin state is given by P_ϕ = 102.03 h (4.25 days), P_ψ = 484.80 h (20.2 days), and the angular momentum vector is pointed at λ = 273.2° and β = +15.8°. The long-axis rolling angle A_ψ oscillates between −42° and +42°. The period of nutation of the long axis P_θ is the same as P_ψ, and the nodding amplitude A_θ is 11°.

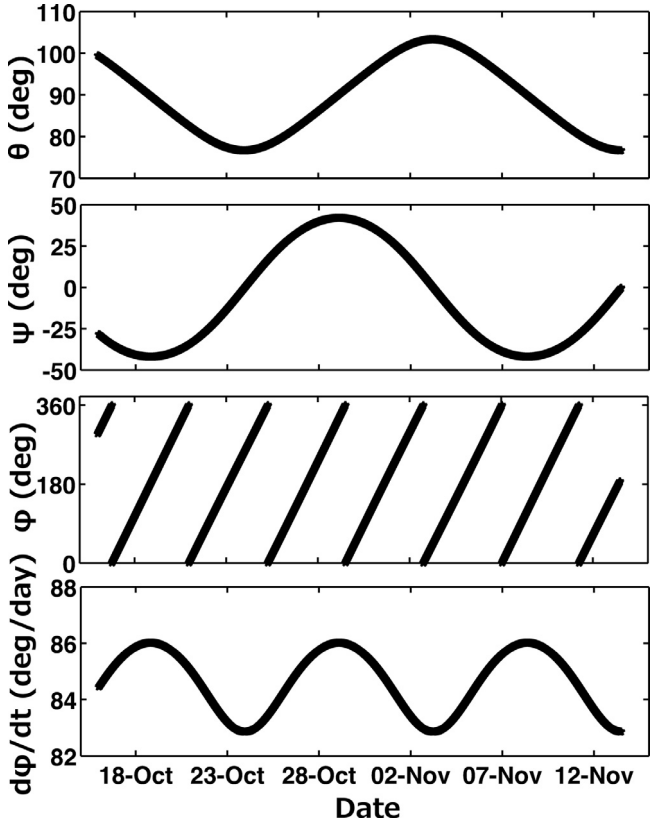

Fig. 5. The Euler angles θ, ψ, and ϕ that describe the SAM NPA spin state during the Goldstone observations between October 16 and November 13. For a SAM spin state, θ is the nodding amplitude of the long axis with respect to the total rotational angular momentum vector, ψ is the rolling amplitude about the long axis, and ϕ is the rotation angle of the long axis about the angular momentum vector, the only angle that circulates. The periods of the Euler angles are: $P_\phi = 4.26$ days and $P_\psi = P_\theta = 20.55$ days. (P_ϕ is an average period.) The rotation rate $d\phi/dt$ of the long axis about the angular momentum vector varies by only a few percent and has a period of $P_\psi/2$.

We proceeded with a 10th order spherical harmonics model that provides much more flexibility in fitting the complex shape. This produced a significant improvement to the fits (reduced χ^2 of 1.046) with respect to the PA spin state (reduced χ^2 of 1.108; compare Supplementary Figs. 3 and 7). Supplementary Table 4 lists the physical properties of SAM harmonic shape model.

We then converted the 10th order spherical harmonics model into a vertex model parameterized with 10,340 triangular facets. At this advanced stage of shape modeling, we used *Shape* to optimize both the model's shape and spin state. Each facet has a mean edge length of 39 m. The model resolution is ~10 times coarser that the finest imaging resolution of 3.75 m, but given that high-resolution images do not show any obvious fine scale surface structure, 39 m resolution was sufficient and practical. Increasing the model resolution to below 10 m would result in more than 140,000 facets that would significantly slow down the shape modeling process without obvious benefits. The spin state adjustments were very minor at this stage of the modeling. The entire process was guided by the set of penalties (described in Magri et al., 2007) that ensured uniform density and an overall smooth appearance of the small-scale surface features.

The NPA rotation can be visualized by following the time evolution of Euler angles ϕ, θ, ψ, and $d\phi/dt$ (Fig. 5), where $d\phi/dt$ is the rate at which the long axis rotates about the angular momentum vector. Table 4 lists the properties of the model and spin state parameters. The angular momentum vector points toward ecliptic longitude and latitude $(273.6 \pm 10, +16.9 \pm 5)°$. We estimated 3-$\sigma$ errors based on perturbing the Euler angles, spin state, and moments of inertia, and by observing if the offsets produce any visible changes in the fits (Supplementary Fig. 8). The final spin state has an average period of rotation of the long axis about the angular momentum vector $P_\phi = 4.26 \pm 0.02$ days. The period of oscillation about the long axis P_ψ is 20.86 ± 3.75 days. P_θ is the same as P_ψ and the nodding amplitude $A_\theta = 13 \pm 2°$.

Table 4
Physical properties of the 2007 PA8 model.

Principal axes:		
X	1.82 ± 0.09 km	(5% uncertainty)
Y	1.32 ± 0.07 km	(5% uncertainty)
Z	1.14 ± 0.17 km	(15% uncertainty)
Axis ratios:		
X/Y	1.38 ± 0.10	
Y/Z	1.16 ± 0.16	
Equivalent diameter:	1.35 ± 0.07 km	
Surface area:	6.17 ± 0.59 km^2	
Volume:	1.30 ± 0.21 km^3	
DEEVE:		
X	1.79 ± 0.05 km	
Y	1.26 ± 0.04 km	
Z	1.10 ± 0.17 km	
Spin state at epoch Nov 13 2012, 11:32:18 UTC:		
$\phi_0 = 186.1 \pm 10°$, $\theta_0 = 76.7 \pm 10°$, $\psi_0 = -0.3 \pm 10°$		
$W_l = 32.8 \pm 1.0°$/day, $W_i = -0.5 \pm 5.0°$/day, $W_s = 80.6 \pm 0.3°$/day		
$I_l/I_s = 0.582 \pm 0.058$, $I_i/I_s = 0.921 \pm 0.015$ (dynamical moments of inertia)		
Optical albedo:	$p_V = 0.29 \pm 0.14$	
OC radar albedo:	$\eta_{OC} = 0.14 \pm 0.05$	

"DEEVE" stands for dynamically equivalent, equal volume ellipsoid. Equivalent diameter represents a sphere with the same volume as the shape model. The dynamical moments of inertia ratios are consistent with (within 0.15%) rotation of a uniform density object.

3.2.2. LAM NPA spin state fits

Although the SAM NPA model provided good agreement with the data, we also explore the possibility that the data could also be fit with a LAM NPA spin state. In order for LAM to provide good fits, it has to produce similar plane-of-sky and instantaneous spin-vector orientations as the SAM state. The SAM NPA solution showed that the asteroid rotated ~ 84° about the long axis between October 29 and November 8. For LAM, the amount of rotation should be similar, except the rotation would continue until one full cycle is completed ~ 33 days later. Thus, this was a relatively constrained LAM NPA search: we were looking for a spin state with P_ϕ ~ 4 days and P_ψ ~ 43 days.

The Euler angles, rates, and the moments of inertia were initialized in the same manner as for the SAM search. Supplementary Fig. 5 shows the eight-dimensional phase space covered by 500 LAM spin state candidates. Supplementary Table 3 ranks the 20 best χ^2 scores. The fit with $P_\phi = 102.62$ h (4.28 days) and $P_\psi = 952.48$ h (39.69 days) provides the best match to the data (Supplementary Fig. 6). This model was refined with a 10th order spherical harmonic shape (Supplementary Fig. 7 and Supplementary Table 4), but the resulting reduced χ^2 did not approach the equivalent SAM fit (1.139 vs 1.046). The mismatches are evident in both the echo bandwidths and the shapes of the leading edges. Thus, we favor the SAM model to describe 2007 PA8's rotation.

3.3. Fit to the data

Fig. 6 shows the best shape model fits to selected delay-Doppler images and Fig. 1 shows fits to the echo power spectra. Fits to all the delay-Doppler images appear in Supplementary Fig. 9. The fits match the bandwidths, visible extents in time delay, shapes of the

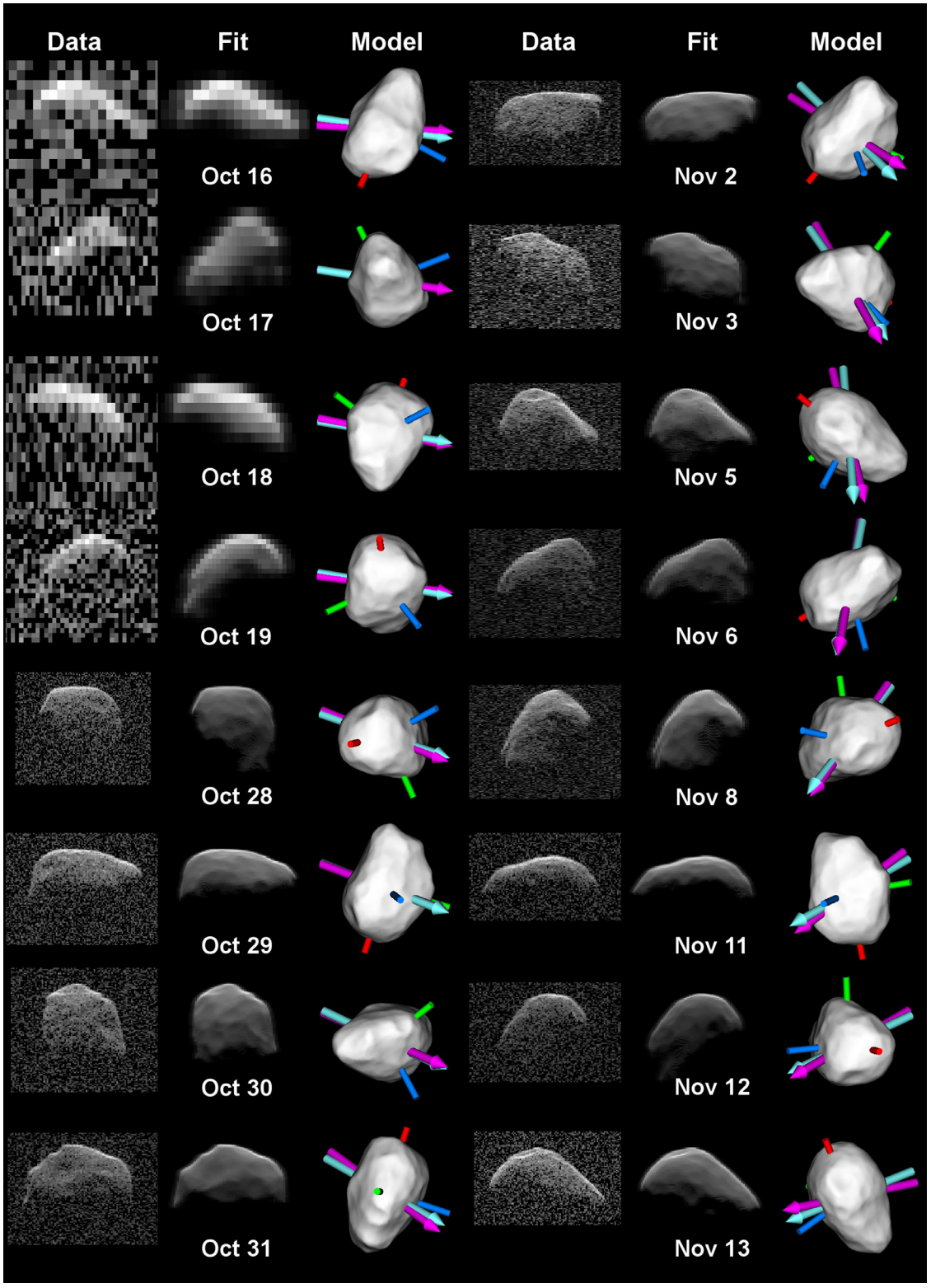

Fig. 6. Collage of, from left to right: delay-Doppler radar images, fits (synthetic images), and plane-of-sky renderings of the vertex shape model. In the data and fits, time delay increases from top to bottom, and Doppler frequency increases from left to right. The plane of sky view is contained in a 2.3 km × 2.3 km square with 301 × 301 pixels. The magenta arrow shows the orientation of the spin vector, the cyan arrow is the angular momentum vector, and the red, green, and blue shafts denote the positive ends of the long, intermediate, and short principal axes. (For interpretation of the references to colour in this figure legend, the reader is referred to the web version of this article.)

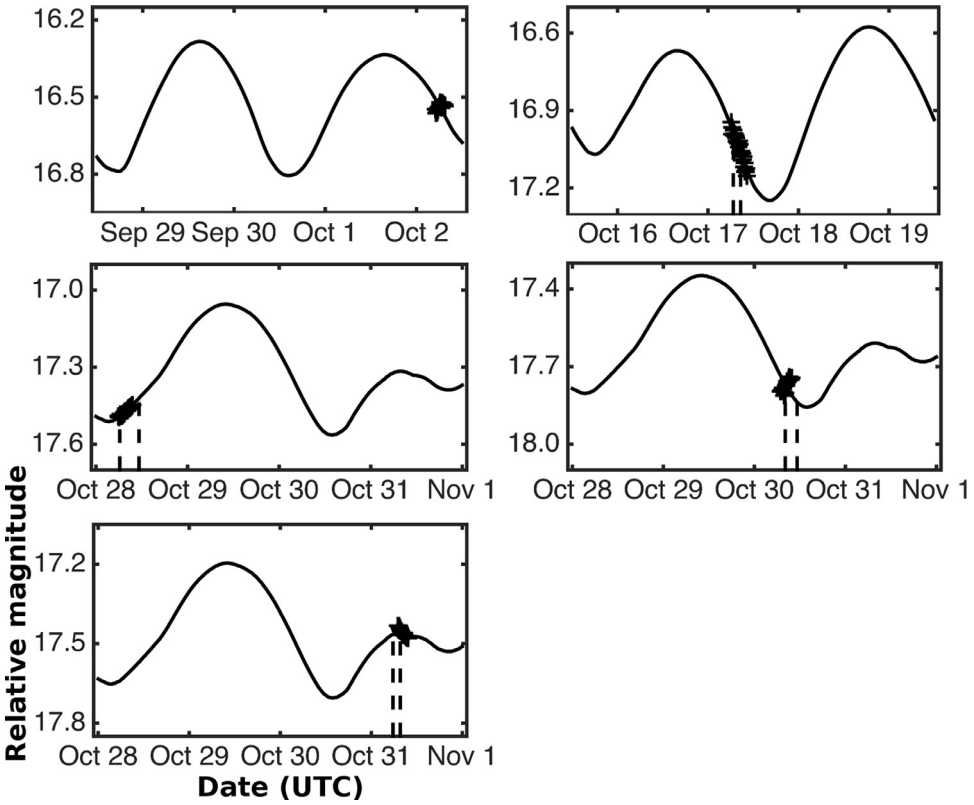

Fig. 7. R-band lightcurves (observations marked with crosses) obtained at Table Mountain Observatory from October 2 to October 31, 2012. The lightcurves were corrected for geocentric and heliocentric distances (1 au from the Sun and 1 au from Earth). The solid lines show synthetic lightcurves produced from the nominal shape model. We used a weighted average of Lommel-Seeliger and Lambert scattering for the optical scattering law. The dashed lines mark the duration of radar observations on the days when lightcurves were observed. October 2 is the only day with no radar observations.

leading edges, prominent surface features, and orientations. Estimating the spin state was the most difficult aspect of shape modeling and without several weeks of radar imaging this might not have been possible.

The fits to the lightcurves are shown in Fig. 7. These are very short lightcurves that cover $<4\%$ of the fastest period ($P_\phi = 4.26 \pm 0.02$ days), and they show <0.1 mag changes. To speed up the fits, we averaged the lightcurve measurements to represent 0.5° of rotation, assuming $P_\phi \sim 102$ h.

Fig. 7 shows the lightcurve data superimposed on synthetic lightcurves with a period of 4 days to provide some context. A close-up view is shown in Supplementary Fig. 10. The lightcurve from October 2 is the only one obtained outside the interval of radar observations. On Oct. 2, 2007 PA8 was more than 0.24 au from Earth and the lightcurve was taken only 23° from the 96% full Moon. The lightcurve is also very short, so it is difficult to estimate the fit quality. The magnitude increase appears to conflict with the downward trend in the synthetic lightcurve, so this could signal an issue with the reported spin state, shape, or a problem with the lightcurve data.

The other lightcurves were obtained at times that overlap the radar observations. Our shape model produced good fits to the October 17, 28, and 31 lightcurves, but the fit on October 30 shows a decreasing trend that differs from the data. High-resolution delay-Doppler images on October 30 at overlapping times fit well (Fig. 6), so it is not clear why the same model does not also match the lightcurve. Hudson and Ostro (1998) encountered a similar situation when they fit lightcurves for (4179) Toutatis with its radar derived shape model and spin state. Hudson and Ostro found that the root-mean-square (rms) of the residuals for the Toutatis lightcurves was a relatively large, 0.12 mag, which they argued originates from systematic errors in the data because slow, NPA rotation makes obtaining well-calibrated lightcurves difficult.

We first tested if the LAM model from Supplementary Fig. 7 provides a better fit to the lightcurves, but given that the LAM and SAM orientations closely follow each other, there were no improvements to the fits (Supplementary Fig. 11). We next tried to adjust the nominal SAM spin state and/or shape model to better match the lightcurves on October 2 and 30, but this resulted in degradation of the radar fits. Finally, we modeled albedo variation across the surface and found that a heterogeneous albedo distribution with rms of 0.25 can match the lightcurves (Supplementary Figs. 12 and 13). Albedo variations have been found on two main belt asteroids visited by spacecraft: (951) Gaspra (Beltonet al. 1992; Helfenstein et al. 1994) and (4) Vesta (Li et al, 2015). Furthermore, Hudson et al. (1997) found a much better match to their lightcurves fit for (4769) Castalia if they considered a non-uniform albedo distribution.

3.4. Shape of 2007 PA8

Fig. 8A shows principal axis views of the shape model and Table 4 list its physical properties. The radar observations provided excellent rotational coverage and a variety of viewing geometries that resulted in a shape with small uncertainties. The asteroid is asymmetric along the long axis in the sense that one end is significantly wider and more rounded than the other, and the shape is also asymmetric along the intermediate axis. 2007 PA8 is similar in shape to (2100) Ra-Shalom (Shepard et al., 2000), (4660) Nereus (Brozović et al., 2009), and Apophis (Pravec et al, 2014).

The shape model size uncertainties were estimated using both visual and statistical methods. We evaluated the quality of the fits as we scaled the nominal shape model. Visual inspection produced

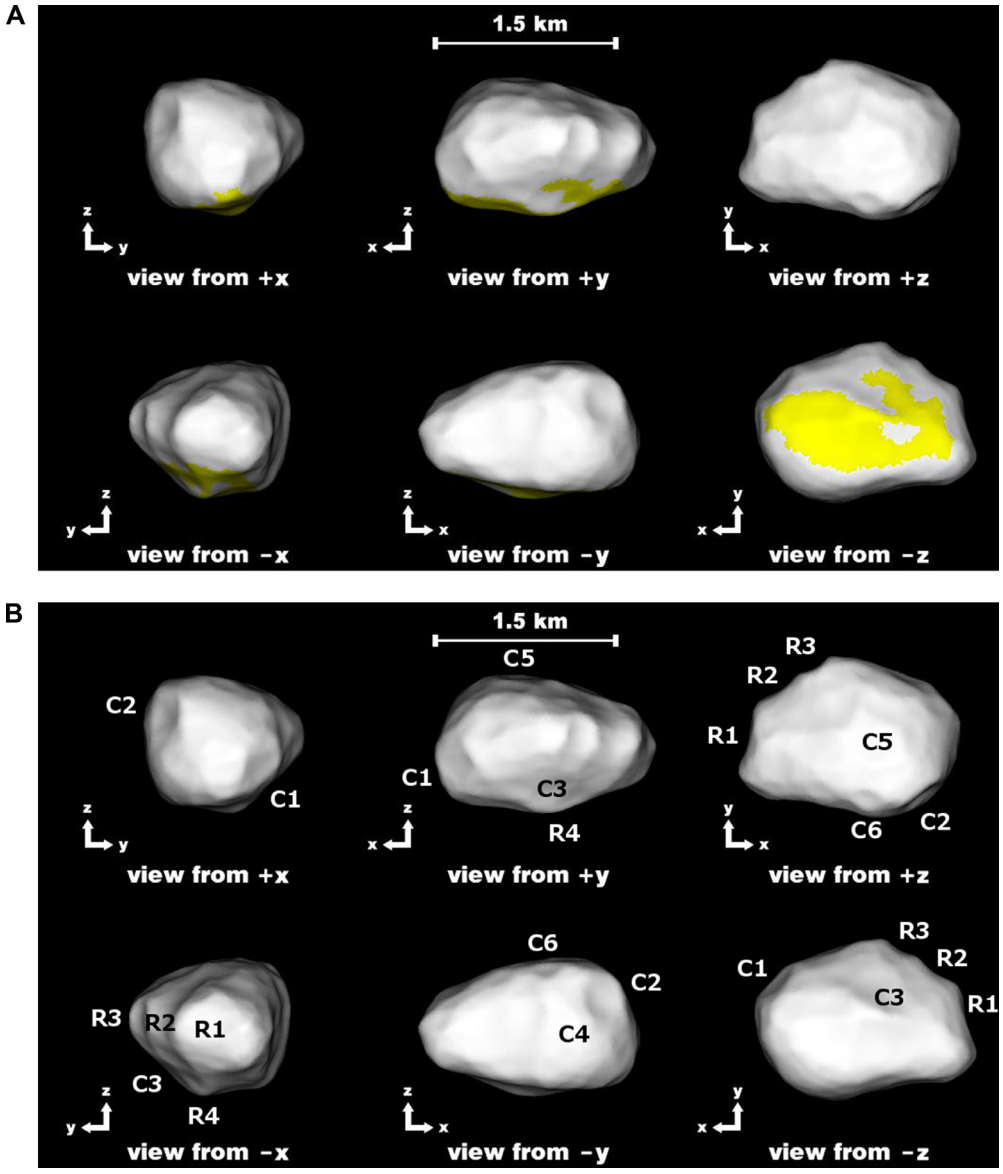

Fig. 8. A. Principal-axis views of the shape model. The model has 5172 vertices that form 10,340 triangular facets with mean edge length 39 m. Yellow shading indicates areas that are not well constrained by the data because the radar incidence angle was always greater than 60°. The model has DEEVE dimensions of 1.79 km × 1.26 km × 1.10 km. **B.** Same as **A** but with letters highlighting features discussed in the text.

uncertainties that were about twice as large as the bounds calculated from a statistically significant increase in χ^2 (Eq. (3) in Fang et al. 2011; originally in Press et al., 2007). We list more conservative uncertainties in Table 4. We found that the length changes of the model's principal x or y axes of more than 5% produced visible mismatches in the fits. The uncertainty is somewhat larger (15%) for the z principal axis because the observations did not fully constrain the region near the south pole.

The uncertainties of the model's principal axes are: X = 1.82 ± 0.09 km, Y = 1.32 ± 0.07 km, and Z = 1.14 ± 0.17 km, with an equivalent diameter of 1.35 ± 0.07 km. The ratio of x- and y- axes is X/Y = 1.30 ± 0.10 which indicates that 2007 PA8 is moderately elongated relative to the NEA population sampled by radar (available at: http://echo.jpl.nasa.gov/~lance/nea_elongations.html).

Fig. 8B highlights numerous features on the model. C1 and C2 are approximately circular, relatively shallow concavities and could be considered as candidate craters. Feature C3 is a depression formed by the upward slope of a ridge and does not have a rounded shape. The shape model contains other smaller concavities, 50–100 m in diameter such as features that we labeled C4, C5, and C6 in Fig. 3B. These concavities are subtle but identifiable with feature C4 being the most difficult to spot due to lighting conditions in Fig. 8B. We used *Shape* to create graphical output that highlights the mapping from model surface elements to delay-Doppler space to confirm that we have correctly identified the shape model features.

We have also identified candidate ridges (labeled R1, R2, R3, and R4) by inspection of the model. R1, R2, and R3 are narrow regions that give an almost saw-tooth appearance when the object is viewed from the −z or +z directions. The entire +y side of the asteroid is sloped and relatively narrow along the z-axis, and R1, R2, and R3 form a ridge along ~ 1/4th of the asteroid's circumference. They are particularly visible in delay-Doppler images from October 28 and 29 when the leading edge appears almost serrated (Fig. 6). R4 is the ridge that contributes to the central part of the trailing edge of the echoes on October 30 and 31. The fact that we can see

Table 5
Disk-integrated properties.

Date	Time range (UTC) START STOP	Resolution (Hz)	Runs	Looks	σ_{OC} (km^2)	SC/OC	Area (km^2)	η_{OC}
Oct 16	06:37:10–07:02:54	0.5	6	374	0.22	0.21 ± 0.05	1.570	0.14
Oct 17	06:43:14–07:12:06	0.5	7	416	0.20	0.39 ± 0.06	1.290	0.16
Oct 18	05:44:13–06:16:40	0.5	5	282	0.18	0.24 ± 0.06	1.549	0.12
Oct 19	06:11:04–06:29:17	0.5	5	268	0.26	0.28 ± 0.04	1.542	0.17
Oct 28	06:20:10–06:28:17	0.5	4	119	0.18	0.34 ± 0.02	1.354	0.13
Oct 29	05:06:08–05:15:51	0.5	5	138	0.26	0.26 ± 0.02	1.784	0.15
Oct 31	05:51:05–05:59:31	0.5	5	108	0.18	0.34 ± 0.02	1.606	0.11
Nov 02	07:00:56–07:08:15	0.5	5	98	0.21	0.25 ± 0.02	1.717	0.12
Nov 03	08:11:18–08:18:16	0.5	5	91	0.18	0.33 ± 0.01	1.453	0.12

Disk-integrated OC radar cross section (σ_{OC}) and circular polarization ratio (SC/OC) estimated from echo power spectra. Resolution in Doppler frequency was chosen in order to provide enough looks to obtain Gaussian noise statistics. The number of looks represents the number of statistically independent measurements that were used to get the average SC and OC spectra. OC radar albedo (η_{OC}) is calculated by dividing the radar cross section (σ_{OC}) by the model's projected surface area.

so far in the back suggests that the sloped surface of R4 is real, but R4 is in a region that was viewed only at high incidence angle (almost 60°), so it is important to be cautious when interpreting the shape model in this area.

3.5. Optical albedo

We estimate the visual geometric albedo based on the equivalent diameter from the shape model and an absolute visual magnitude of $H_v = 16.30 \pm 0.52$ that was calculated as an unweighted average of 612 photometric observations obtained between July 2002 and May 2013 that are available via the JPL Horizons website (http://ssd.jpl.nasa.gov/horizons.cgi). The optical albedo was calculated using the expression $p_v = (1329/D)^2 \times 10^{-0.4Hv}$ (Pravec and Harris, 2007), giving $p_v = 0.29 \pm 0.14$. The uncertainty was obtained by propagating the errors in D and H_v. Our results imply that 2007 PA8 is optically bright; this albedo is consistent with the Q taxonomy reported in Fornasier et al. (2015).

4. Orbit refinement

During the observations, we estimated delay-Doppler corrections to the ephemerides by eye and generated new orbital solutions as needed. We later used the 3D model and its much smaller uncertainties in the center-of-mass location to refine the astrometry. We obtained 15 delay and 26 Doppler measurements (Supplementary Table 5) that were combined with 635 optical astrometry measurements spanning 2002 Jul 13–2013 May 13 to calculate JPL/Horizons orbit solution 157. The original radar astrometry estimated during the observations was excluded from the solution. The orbital elements based on solution 157 are listed in Supplementary Table 6. For this multi-apparition case, the Earth minimum orbit intersection distance (MOID) and Earth encounter predictability did not change with the addition of the radar astrometry.

2007 PA8 makes more than 20 flybys within 0.045 au of Earth and 8 flybys within 0.025 au of Mars during 1220 years of reliable orbital estimates (Supplementary Table 7). The asteroid also approaches within 1.5 au of Jupiter and it closely encounters at least two of the sixteen most massive main-belt asteroids: 16 Psyche (within 0.039 au in 2079) and 52 Europa (within 0.042 au in 2525).

5. Disk-integrated properties

Table 5 lists disk-integrated properties for 2007 PA8. The mean circular polarization ratio SC/OC is 0.29 ± 0.06. The mean SC/OC for 214 near-Earth asteroids studied by Benner et al. (2008) is 0.34 ± 0.25, suggesting that the near-surface roughness for 2007 PA8 at decimeter spatial scales is comparable to the mean. Q and S-class NEAs have a mean SC/OC = 0.27 ± 0.08 (N = 70), indicating that 2007 PA8 fits well within this distribution. This ratio is comparable to the values seen for Toutatis (Ostro et al., 1999; Magri et al., 2001, see also Table 3 in Nolan et al., 2013) and (25143) Itokawa (Ostro et al., 2004), suggesting similar structural complexity, but larger than the values of 0.18 ± 0.03 (12.6 cm wavelength) and 0.14 ± 0.03 (3.5 cm wavelength) measured for (101955) Bennu (Nolan et al, 2013), the target of the OSIRIS-Rex mission.

The SC/OC ratio for 2007 PA8 varied by nearly a factor of two on the first two days of observing, with values of 0.21 ± 0.05 on October 16 and 0.39 ± 0.06 on October 17. The ratios after October 28 have smaller uncertainties and Table 5 shows variations of 20–30% from the average. It is difficult to establish if there are systematic variations in SC/OC across the surface of 2007 PA8 given that the Doppler-only data are relatively sparse and the object is in a complex state of a rotation. We also checked SC/OC delay-Doppler images on the days when the data were available in both channels and they showed no evidence for SC/OC surface heterogeneity (Supplementary Fig. 14).

The mean OC radar cross section is $\sigma_{OC} = 0.21 \pm 0.07$ km^2. Due to systematic calibration and pointing errors at Goldstone, we assign uncertainties in the radar cross section of ~ 35%. The OC radar albedo is calculated by dividing the mean OC cross section by the mean projected area of the model. We obtain a radar albedo of $\eta_{OC} = 0.14 \pm 0.05$ that is consistent with the average value of $\eta_{OC} = 0.15 \pm 0.06$, reported for 21 S-class NEAs (http://echo.jpl.nasa.gov/~lance/asteroid_radar_properties/nea.radaralbedo.html).

6. Gravitational environment

The shape model enables us to investigate the gravitational environment with an assumption of a homogeneous density (Scheeres, 2012). The gravitational slope is defined as the angle between the tangent plane to the surface and the total gravitational acceleration at a given location on the body. The geopotential can be defined as the gravitational potential energy across the surface of the body, and when combined with the kinetic energy of a particle, it constitutes the total energy of the system. The asteroid's geopotential and slopes are insensitive to the total density due to the extremely slow rotation rate of the body. Thus, modeling the complex rotation state for this asteroid does not change these results in an observable way, so we have analyzed the geopotential and gravitational slopes without adding the rotation. In the following we have assumed a density of 2 g/cm^3, but the slope results are in fact independent of this (without the rotation being added), and the geopotential results are relatively independent of this.

Figs. 9A and B map the gravitational slopes on the surface and plot the slope distribution across the body. 2007 PA8 has a maximum slope of 34.5° and a mean slope of 12°. These are relatively

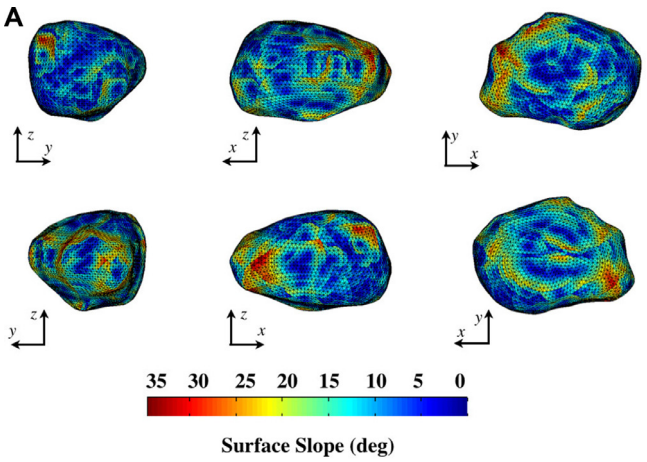

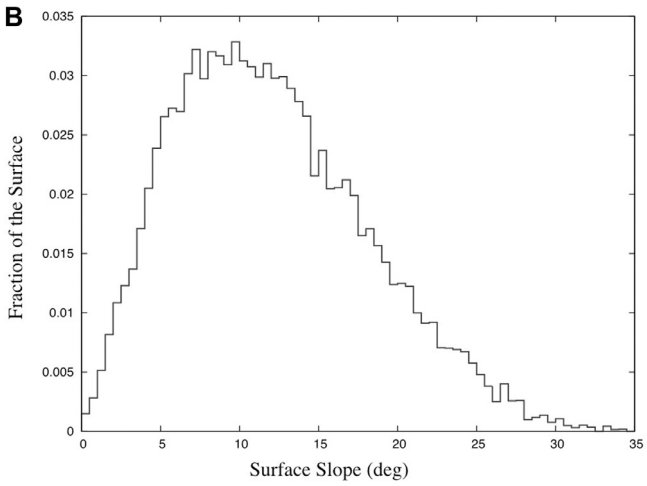

Fig. 9. A. Gravitational slopes assuming a uniform density of 2 g/cm^3. **B.** Histogram showing the fraction of the surface with a particular gravitational slope value, binned every 0.5° in slope angle.

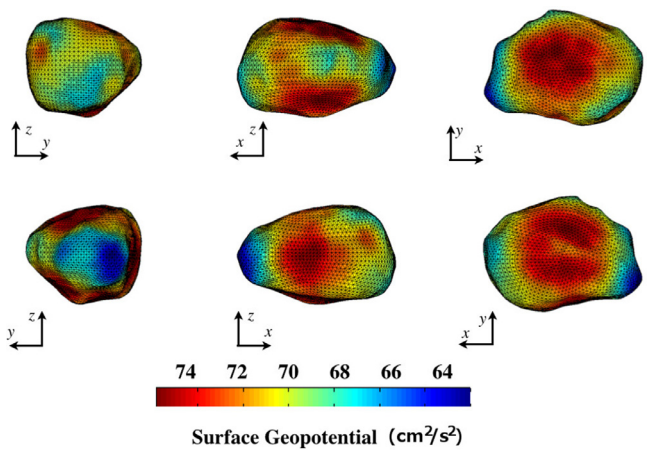

Fig. 10. Surface geopotential assuming a uniform density of 2 g/cm^3. Loose material would tend to flow from blue to red regions.

moderate slopes, so there is no evidence that granular material on the surface of 2007 PA8 needs to have any cohesiveness or tensile strength (Holsapple, 2001, 2004). The slope is distributed heterogeneously across the body, and shows several distinct regions that have a maximum slope of over 30° (Fig. 9A). The most prominent high slope region is inside the C2 indentation. A second, more global, feature evident from the slope map is a ridge of higher slopes encircling the smaller end.

Additional insight can be gleaned by observing the surface potential mapped across the surface, shown in Fig. 10. The surface potential is the square of the equivalent speed that a particle would have if dropped from infinity to the surface. Thus, a higher speed denotes a point that is lower in the geopotential, and vice-versa. There are five major potential lows on the body. First, as expected for a slow rotator, the two polar regions (+z and –z views) are both geopotential lows. In addition, the equatorial indentation (–y view, bottom-middle) is also seen to be a geopotential low, with the equatorial high slope area leading directly into this region. A fourth, small relative low corresponds to concavity C2 located at body-fixed longitude and latitude of 320° and +20°. There is another small high slope region along the equatorial plane in +y view (top-middle in Fig. 10). This is the area just behind ridge R3.

The geopotential lows all correspond to regions of zero slope across the body surface. These are the areas where we expect to find any loose material that has drained into these regions and settled. When the direction of the slope vectors are mapped across the surface, we find a complex pattern, with drainage regions going toward the poles and toward the nonpolar geopotential lows. The smaller end of the asteroid is relatively high in the geopotential (–x view, bottom-left), with the high slope region corresponding to a region of approximately constant geopotential intermediate between the maximum and minimum values. Taken in its entirety, these features could support the hypothesis that the small end of the asteroid has undergone erosion. This could explain its angular appearance and tapered shape when compared to the more rounded end. There are at least two possible explanations for the existence of the large equatorial geopotential low in the –y view: this could be an interface between two components resting on each other, or alternatively, this could be evidence for a hidden crater that was filled by loose material.

7. Discussion

7.1. Origin of 2007 PA8's NPA spin state

What is the origin of 2007 PA8's excited spin state? Although a detailed simulation of how 2007 PA8 entered a SAM state is beyond the scope of this paper, we still discuss some plausible mechanisms.

Vokrouhlický et al. (2007) explored a possible connection between the Yarkovsky–Radzievskii–O'Keefe-Paddack (YORP) thermal radiation effect (Rubincam, 2000) and the onset of tumbling rotation. They found that bodies whose spin state slowed significantly due to the YORP effect reach a point when the object starts to tumble. The onset of non-principal axis rotation is correlated with thermal properties and the effects of internal energy dissipation. 2007 PA8 is a slow rotator, so YORP is a plausible mechanism for its current spin state.

Henych and Pravec (2013) found that asteroid rotation can transition into an excited state due to subcatastrophic impacts where the onset and a degree of tumbling is determined by the ratio of the projectile's orbital angular momentum and the target's rotational angular momentum. 2007 PA8's surface has features that can be interpreted as impact craters. The largest candidate crater, feature C2, is ~ 400 m in diameter and it resembles some of the test cases that caused the onset of tumbling rotation in the simulations discussed in Henych and Pravec (2013). The large geopotential low at the equator (Fig. 10) also raises the question if there was another, much larger impact crater that has been obscured by mate-

Table 6
NEAs detected with radar with Tisserand parameter T < 3.

Asteroid	Name	T	H (mag)	Date	Obs.	D (km)	Taxonomic class	References
	2006 AL8	2.157	18.4	Feb 2012	A	–	–	Taylor et al., unpub.
	2012 FZ23	2.367	18.2	Mar 2012	A	~0.6	Likely not dark	Nolan et al., unpub.
(410778)	2009 FG19	2.391	18.1	Sep 2014	G	> 1.2	–	Brozovic et al., unpub.
						(1.46 ± 0.57)	Dark	Nugent et al. (2015)
(163732)	2003 KP2	2.634	15.4	Oct 2003	A	> 2	–	Taylor et al., unpub.,
							C	DeMeo and Binzel (2008)
(139359)	2001 ME1	2.671	16.6	Jun 2014	A	–	P	Rivkin et al. (2005)
	2011 LC19	2.677	18.9	Oct 2011	A + G	> 1.0	Likely dark	Brozovic et al., unpub.
	2009 KC3	2.728	18.0	Aug 2009	A + G	1.2	–	Taylor et al. (2010),
							C, Xe, X	Hicks et al. (2009a)
(170502)	2003 WM7	2.745	17.2	Dec 2011	A	~1.8	Likely dark	Nolan et al., unpub.
	2016 LX48	2.748	19.4	Sep 2016	A + G	~0.8	Likely dark	Rivera-Valentin et al., unpub.
	2014 DJ23	2.763	22.4	Mar 2014	A	0.24	Likely dark	Taylor et al., unpub.
	2005 AB	2.792	17.5	Feb 2005	A	~1.9	Likely dark	Reddy et al. (2006),
							C	DeMeo and Binzel (2008)
	2011 BX18	2.793	18.1	Aug 2016	A	(3.0±0.7)	Dark	Mommert et al. (2015)
(217796)	2000 TO64	2.801	17.0	Nov 2009	A	> 0.6	–	Taylor et al., unpub.,
							Sq, Sk, S	Hicks et al. (2009b,c)
							S	Somers et al. (2010),
							Sr	Thomas et al. (2014),
							S/Sr	DeMeo et al. (2014),
	2010 PR66	2.817	19.3	Jul 2015	A	~0.45	–	Taylor et al., unpub.,
						(0.68±0.02)	Dark	Masiero et al. (2015)
	2014 EL45	2.818	19.9	Mar 2014	A	0.45	Likely dark	Taylor et al., unpub.,
(214088)	2004 JN13	2.844	15.3	Dec 2014	A	1.8	–	Taylor et al., unpub.,
						(2.97)	–	Trilling et al. (2010),
							Sq	Thomas et al., (2014)
(192642)	1999 RD32	2.871	16.3	Mar 2012	A + G	~5.0	Likely dark	Nolan et al., unpub.
	2014 JL25	2.878	23.0	May 2014	A + G	~0.3	–	Brozovic et al., unpub.,
						(0.23 ± 0.06)	Dark	Nugent et al. (2015)
	2012 RV16	2.893	19.6	Oct 2012	A	–	S-complex	Howell et al., unpub.
	2010 JL33	2.907	17.7	Dec 2010	G	(1.78±0.03)	Dark	Mainzer et al. (2011), Mommert et al. (2015)
	2014 EQ12	2.907	21.1	Mar 2014	A	> 0.3	Likely dark	Howell et al., unpub.
	2014 UF206	2.912	18.8	Jan 2015	A	1.2	Likely dark	Taylor et al., unpub.
	2012 JS11	2.915	20.3	Sep 2012	A	~0.75	Likely dark	Howell et al., unpub.
	2016 JD18	2.921	24.7	May 2016	G + GBT	> 0.05	Likely dark	Naidu et al., unpub.
(14827)	Hypnos	2.933	18.3	May 1986	G	1–2	Likely dark	Ostro et al. (1989),
							C	Wisniewski et al. (1987)
	2010 UM7	2.933	27.6	Oct 2010	A	> 0.05	Likely dark	Howell et al., unpub.
	2002 FC	2.936	18.9	Jun 2002	A + G	~0.7	Likely not dark	Nolan et al., unpub.
(214869)	2007 PA8	2.947	16.4	Oct 2012	G	1.35	Likely not dark	this paper,
							Q	Fornasier et al. (2015)
							Q/O	Kuroda et al. (2014),
							Xc	Hicks et al. (2012a)
							X	Godunova et al. (2013)
	2012 HM8	2.953	24.0	Apr 2012	A	0.06	Likely not dark	Taylor et al., unpub.,
	2008 SV11	2.958	18.4	Mar 2009	G + A	0.8	–	Taylor et al., unpub.,
							CX	Somers et al. (2010)
	2002 CX58	2.959	22.3	May 2016	A	0.13	Likely not dark	Fernandez et al. (2005)
	2015 TB145	2.982	20.0	Oct 2015	A + G + GBT	~0.4	–	Busch et al., unpub.,
							Dark	NASA press release[a]
	2015 FL	2.985	20.8	Apr 2015	A	~0.1	Likely not dark	Howell et al., unpub.
(53319)	1999 JM8	2.987	15.2	Jul 1999, May 2008	A + G, A	~5.0	Likely dark	Benner et al. (2002),
							X	Binzel (2004),
							P	DeMeo and Binzel (2008)
(329614)	2003 KU2	2.988	17.6	Jul 2012	A	~1.0	–	Taylor et al., unpub.,
							Sq	Hicks et al. (2012b)

We list the object's Tisserand parameter, T, absolute magnitude, H, observing date, observatory code, A = Arecibo and G = Goldstone, GBT = Green Bank Telescope, diameter estimated from radar data when available, diameter estimated from non-radar sources (e.g. thermal modeling; listed in brackets), and taxonomic class. The objects are ranked by the increasing Tisserand parameter.

[a] http://www.jpl.nasa.gov/news/news.php?feature=4760

rial migrating from the neighboring region that is on a geopotential high. The most likely time and place for 2007 PA8 to receive an impact would be during one of its passages though the main belt.

Scheeres et al. (2000) studied how breakup of a parent body and the subsequent gravitational interactions among the fragments can cause an asteroid to spin-up, spin-down, or tumble. They also investigated how certain dynamical events can "decide an asteroid's rotational state for most of its life". Their analysis studied the changes in asteroids spin states due to exceptionally close flybys within a few radii of the terrestrial planets. Their conclusions were that proximity, orbital geometry, and spin axis orientation play critical roles in the onset of NPA rotation. 2007 PA8 makes relatively close approaches, within ten lunar distances, of Earth and Mars during the interval of reliable orbit estimation, but this is too distant to excite its spin state. However, closer planetary flybys could have occurred in the past. A more thorough investigation would require long-term orbital integrations.

How long would it take 2007 PA8's excited spin state to damp back to pure PA rotation? The time for asteroid nutational damping can be expressed as (Pravec et al., 2014):

$$T_d = \frac{P_{obs}^3}{C^3 D_m^2} \quad (6)$$

where C is a constant equal to 36 or 33, depending on the proposed mechanism of energy dissipation due to stress-strain cycling within the tumbling body; P_{obs} is the period of rotation in hours; D_m is the diameter in km; and T_d is the time in Gy. Pravec et al. calculated the constant C by assuming elastic modulus $\mu = 10^9$ Pa, tidal quality factor Q = 100, and density $\rho = 2$ g/cm^3. These are all reasonable values for a small body, but all three quantities have large uncertainties. Taken at face value, Eq. (6) implies that 2007 PA8 has a damping time of $T_d > 12.5$ Gy.

A recent study by Scheirich et al. (2015) estimated the elastic modulus and quality factor for binary NEA (175706) 1996 FG3. 1996 FG3 is apparently in an equilibrium between the binary YORP effect and tidal damping, and as a result, Scheirich et al. estimated $\mu Q = 2.7 \times 10^9$ Pa. Using that value for 2007 PA8 gives a damping time of $T_d > 340$ MY, or ~ 37 times less than we obtained by adopting values from Pravec et al. (2014). This timescale is still much longer than the YORP timescale, the orbital lifetime, and perhaps the collisional-excitation timescale. Hence, the trigger event for the tumbling motion of 2007 PA8 could have occurred a very long time ago, likely before migration into the near-Earth region.

7.2. NEAs with cometary orbits detected by radar

Approximately 640 NEAs have been observed by radar to date, and 35 of these (5% of the total) have comet-like orbits characterized with Tisserand parameter T < 3.0. For comparison, comets represent a very small subsample of objects detected by radar. Only 19 have been detected and 9 are Jupiter-family comets.

Table 6 lists all the NEAs detected by radar with Tisserand parameter T < 3. These objects represent a diverse population: at least one is a binary (2005 AB), four are contact binaries (2008 SV11, 2002 FC, 1999 RD32, 2014 UF206), three are slow tumblers (1999 JM8, 2003 KP2, 2007 PA8), and five are rapid rotators with periods of less than 5 h (2003 KU2, 2010 UM7, 2012 RV16, 2011 LC19, 2014 UF206, 2016 LX48).

Among the 35 NEAs with T < 3 in the radar sample, at least 24 (~ 69%) are optically dark and at least 10 (~ 29%) are not optically dark. Table 6 suggest there is a significant fraction of optically bright objects in comet-like orbits that are not cometary in origin. This is consistent with the results by Mommert et al. (2015) who found that ~ 50% of NEAs in comet-like orbits have comet-like albedos, implying a mix of objects with different origins.

7.3. Future observing opportunities

Barring major improvements in sensitivity, the next opportunity for radar imaging of 2007 PA8 will occur in October 2084, during an approach within 0.173 au when an Arecibo-equivalent radar system would have SNRs of ~ 600/day. SNRs comparable to those observed in 2012 at Goldstone (~ 4300/day) will next occur in December 2122 during an approach within 0.044 au. 2007 PA8 is a challenging target for ground-based optical observations because it is generally relatively faint and/or at low solar elongations. The next good opportunity for optical observations will occur in 2031 when 2007 PA8 will reach magnitude 18.5 at solar elongations > 140°. Photometric observations lasting several weeks could improve estimates of the spin state.

Acknowledgments

We thank the Goldstone technical and support staffs for help with the radar observations. This work was performed at the Jet Propulsion Laboratory, California Institute of Technology, under contract with the National Aeronautics and Space Administration (NASA). This material is based in part upon work supported by NASA under the Science Mission Directorate Research and Analysis Programs and the Human Exploration and Operations Mission Directorate Advanced Exploration Systems Program. Co-author M. W. Busch was partially supported by the National Radio Astronomy Observatory's Jansky Fellowship program. We thank two anonymous reviewers for suggestions that improved this manuscript.

Supplementary materials

Supplementary material associated with this article can be found, in the online version, at doi:10.1016/j.icarus.2016.10.016.

References

Belton, et al., 1992. Galileo encounter with 951 Gaspra: first pictures of an asteroid. Science 257, 1647–1652.
Benner, L.A.M., et al., 2002. Radar observations of asteroid 1999 JM8. Meteorit. Planet. Sci. 37, 779–792.
Benner, L.A.M., et al., 2008. Near-Earth asteroid surface roughness depends on compositional class. ICARUS 198, 294–304.
Benner, L.A.M., Busch, M.W., Giorgini, J.D., Taylor, P.A., Margot, J.L., 2015. Radar observations of near-Earth and main-belt asteroids. In: Michel, P., DeMeo, F.E., Bottke, W.F. (Eds.), Asteroids IV. Univ. of Arizona Press, Tucson, USA, pp. 165–182.
Binzel, R.P., et al., 2004. Observed spectral properties of near-Earth objects: results for population distribution, source regions, and space weathering processes. ICARUS 170, 259–294.
Brozovic, M., et al., 2009. Radar observations and a physical model of asteroid 4660 Nereus, a prime space mission target. ICARUS 201, 153–166.
Busch, M.W., et al., 2006. Radar and optical observations and physical modeling of near-Earth asteroid 10115 (1992 SK). ICARUS 181, 145–155.
Busch, M.W., et al., 2010. Determining asteroid spin states using radar speckles. ICARUS 209, 535–541.
DeMeo, F.E., Binzel, R.P., 2008. Comets in the near-Earth object population. ICARUS 194, 436–449.
DeMeo, F.E., Binzel, R.P., Lockhart, M., 2014. Mars encounters cause fresh surfaces on some near-Earth asteroids. ICARUS 227, 112–122.
Giorgini, J.D., et al., 1996. JPL's on-line solar system data service. Bull. Amer. Astron. Soc. 28, 1158.
Godunova, V., Reshetnyk, V., Andreev, M., Sergeev, O., Tarady, V., 2013. Spectrophotometric Studies of near-Earth Asteroids at the Terskol Observatory. EGU General Assembly, Vienna, Austria, p. 13797. 2013.
Fang, J., Margot, J.L., Brozovic, M., Nolan, M.C., Benner, L.A.M., Taylor, P.A., 2011. Orbits of near-Earth asteroid triples 2001 SN263 and 1994 CC: Properties, origin, and evolution. Astron. J. 141, 15 154.
Fernández, Y.R., Jewitt, D.C., Sheppard, S.S., 2005. Albedos of asteroids in comet-like orbits. Astron. J. 130, 308–318.
Fornasier, S., Belskaya, I.N., Perna, D., 2015. The potentially hazardous asteroid (214869) 2007 PA8: an unweathered *L* chondrite analog surface. ICARUS 250, 280–286.
Helfenstein, P., et al., 1994. Galileo photometry of asteroid 951 Gaspra. ICARUS 107, 37–60. http://www.sciencedirect.com/science/article/pii/S0019103584710050.
Henych, T., Pravec, P., 2013. Slowly increasing elongations of non-spherical asteroids caused by collisions. Mon. Not. R. Astron. Soc. 545, 1704–1710.
Hicks, M.D., Barajas, T., McAuley, A., 2009a. Broad-band Photometry of the Potentially Hazardous Asteroid 2009 KC3. Astronomer's Telegram, #2247.
Hicks, M.D., et al., 2009b. Long-Slit CCD Spectroscopy of Planetary Radar Targets 1999 AP10, 2000 TO64, and 2000 UJ1. Astronomer's Telegram, #2283.
Hicks, M., Lawrence, K., 2009c. Planetary Radar Targets 1999 AP10, 2000 TO64, 2000 UJ1, and 2000 XK44: Four S-Complex near-Earth Asteroids. Astronomer's Telegram, #2323.
Hicks, M.D., et al., 2012a. Broadband Photometry of 214869 (2007 PA8): A Slowly Rotating Potentially Hazardous Asteroid.
Hicks, M.D., et al., 2012b. Broadband Photometry of the Potentially Hazardous Asteroid 329614 (2003 KU2) Astronomer's Telegram, #4262.
Hicks, M.D., et al., 2014. Spectral diversity and photometric behavior of main-belt and near-Earth vestoids and (4) Vesta: a study in preparation for the dawn encounter. ICARUS 235, 60–74.
Holsapple, K.A., 2001. Equilibrium configurations of solid cohesionless bodies. ICARUS 154, 432–448.
Holsapple, K.A., 2004. Equilibrium figures of spinning bodies with self-gravity. ICARUS 172, 272–303.
Huang, J., et al., 2013. The Ginger-shaped asteroid 4179 Toutatis: new observations from a successful flyby of Chang'e-2. Nat. Sci. Rep. 3 id. 3411.

Hudson, S., 1994. Three-dimensional reconstruction of asteroids from radar observations. Remote Sens. Rev. 8, 195–203.
Hudson, R.S., Ostro, S.J., 1995. Shape and non-principal axis spin state of asteroid 4179 Toutatis. Science 270, 84–86.
Hudson, R.S., Ostro, S.J., Harris, A.W., 1997. Constraints on spin state and hapke parameters of asteroid 4769 castalia using lightcurves and a radar-derived shape model. ICARUS 130, 165–176.
Hudson, R.S., Ostro, S.J., 1998. Photometric properties of asteroid 4179 Toutatis from lightcurves and a radar-derived physical model. ICARUS 135, 451–457.
Kuroda, D., et al., 2014. Visible-wavelength spectroscopy of subkilometer-sized near-Earth asteroids with a low delta-v. Publ. Astron. Soc. Jpn. 66, 5110.
Landau, L.D., Lifshitz, E.M., 1976.). In: Mechanics. Pergamon Press, Oxford, pp. 115–119.
Li, J-L., Helfenstein, P., Burrati, B.J., Takir, D., Clark, B.E., 2015. Asteroid photometry. In: Michel, P., DeMeo, F.E., Bottke, W.F. (Eds.), Asteroids IV. Univ. of Arizona Press, Tucson, USA, pp. 129–150.
Magri, C., Consolmagno, G.J., Ostro, S.J., Benner, L.A.M., Beeney, B.R., 2001. Radar constraints on asteroid regolith compositions using 433 Eros as ground truth. Meteorit. Planet. Sci. 36, 1697–1709.
Magri, C., et al., 2007. Radar observations and a physical model of asteroid 1580 Betulia. ICARUS 186, 152–177.
Mainzer, A.K., et al., 2011. NEOWISE observations of near-Earth objects: preliminary results (albedo and diameters of 428 NEOs). Astrophys. J. 743 (156), 17.
Masiero, J.R., Carruba, V., Mainzer, A., Bauer, J.M., Nugent, C., 2015. The euphrosyne family's contribution to the low albedo near-earth asteroids. Astrophy. J. 809 (179), 8.
Mommert, M., et al., 2015. ExploreNEOs. VII. dormant short-period comets in the near-Earth asteroid population. Astron. J. 150 (106), 9.
Nedelcu, D.A., Birlan, M., Popescu, M., Badescu, O., Pricopi, D., 2014. Evidence for a source of H chondrites in the outer main asteroid belt. Astron. Astrophys. 567 (LL7), 5.
Nolan, M.C., et al., 2013. Shape model and surface properties of the OSIRIS-REx target asteroid (101955) Bennu from radar and lightcurve observations. ICARUS 226, 629–640.
Nugent, C.R., et al., 2015. NEOWISE reactivation mission year one: preliminary asteroid diameters and Albedos. Astrophys. J. 814 (117), 13.
Ostro, S.J., et al., 1989. Radar observations of asteroid 1986 JK. ICARUS 78, 382–394.
Ostro, S.J., 1993. Planetary radar astronomy. Rev. Mod. Phys. 65, 1235–1279.
Ostro, S.J., et al., 1999. Asteroid 4179 Toutatis: 1996 radar observations. ICARUS 137, 122–139.
Ostro, S.J., et al., 2004. Radar observations of asteroid 25143 Itokawa (1998 SF36). Meteorit. Planet. Sci. 39, 407–424.
Pravec, P., Harris, A.W., 2007. Binary asteroid population I. Angular momentum content. Icarus 190, 250–259.
Pravec, P., et al., 2014. The tumbling spin state of (99942) apophis. ICARUS 233, 48–60.
Press, W.H., Flannery, B.P., Teukolsky, S.A., Vetterling, W.T., 2007. Numerical Recipes 3rd edition: The Art of Scientific Computing. Cambridge University Press, New York, USA, p. 780.
Quirk, K., Srinivasan, M., 2013. GSSR Waveforms for Lunar Observations, pp. 1–46 The Interplanetary Network Progress Report, 42-192.
Reddy, V., et al., 2006. Photometric and radar observations of 2005 AB: a new binary near-Earth asteroid. 37th Lunar and Planetary Science Conference abstract 1755.
Rivkin, A.S., Binzel, R.P., Bus, S.J., 2005. Constraining near-Earth object albedos using near-infrared spectroscopy. ICARUS 175, 175–180.
Rubincam, D.P., 2000. Radiative spin-up and spin-down of small asteroids. Icarus 148, 2–11.
Samarasinha, N.H., A'Hearn, M.F., 1991. Observational and dynamical constrains on the rotation of comet P/Halley. ICARUS 93, 194–225.
Samarasinha, N.H., Mueller, B.E.A., 2015. Component periods of non-principal-axis rotation and their manifestations in the lightcurves of asteroids and bare cometary nuclei. ICARUS 248, 347–356.
Sanchez, J.A., Reddy, V., Dykhuis, M., Lindsay, S., Le Corre, L., 2015. Composition of potentially hazardous asteroid (214869) 2007 PA8: an H chondrite from the outer asteroid belt. Astrophys. J. 808 (93), 6.
Scheeres, D.J., Ostro, S.J., Werner, R.A., Asphaug, E., Hudson, R.S., 2000. Effects of gravitational interactions on asteroid spin states. ICARUS 147, 106–118.
Scheeres, D.J., 2012. Orbital Motion in Strongly Perturbed Environments: Applications to Asteroid, Comet and Planetary Satellite Orbiters. Springer-Verlag, Berlin Heidelberg, Germany, pp. 23–59. Springer-Praxis Books in Astronautical Engineering.
Scheirich, P., et al., 2015. The binary near-Earth asteroid (175706) 1996 FG3 — an observational constraint on its orbital evolution. ICARUS 245, 56–63.
Shepard, M.K., et al., 2000. Radar observations of 2100 Ra-Shalom. ICARUS 147, 520–529.
Slade, M.A., Benner, L.A.M., Silva, A., 2011. Goldstone solar system radar observatory: Earth-based planetary mission support and unique science results. Proc. IEEE 99, 757–769.
Somers, J.M., et al., 2010. Optical characterization of planetary radar targets, low-delta V, and potentially hazardous asteroids: results from 2009-2010. Bull. Am. Astron. Soc. 42, 1055.
Taylor, P.A., et al., 2010. Characterization of near-Earth asteroid 2009 KC3 from radar and thermal infrared observations. Bull. Am. Astron. Soc. 42, 1080.
Thomas, C.A., et al., 2014. Physical characterization of warm Spitzer-observed near-Earth objects. ICARUS 228, 217–246.
Trilling, D.E., et al., 2010. ExploreNEOs. I. Description and first results from the warm Spitzer near-Earth object survey. Astron. J. 140, 770–784.
Vokrouhlický, D., Breiter, S., Nesvorný, D., Bottke, W.F., 2007. Generalized YORP evolution: onset of tumbling and new asymptotic states. ICARUS 191, 636–650.
Veverka, J., et al., 2000. NEAR at Eros: imaging and spectral results. Science 22, 2088–2097.
Wisniewski, W.Z., 1987. Photometry of six radar target asteroids. ICARUS 70, 566–572.